

# JGR Solid Earth

## RESEARCH ARTICLE

10.1029/2022JB024445

### Special Section:

Heterogeneity, anisotropy and scale-dependency: Keys to understand Earth composition, structure and behavior

### Key Points:

- Joint inversion of Love and Rayleigh wave phase velocities reveals radial anisotropy (RA) in the upper mantle of the Fennoscandian Shield
- The observed  $\xi$  value of about 1.05 down to at least 200 km is typical for subcrustal continental lithosphere
- AG-type olivine crystal preferred orientation is a possible alternative model to interpret common continental RA

### Supporting Information:

Supporting Information may be found in the online version of this article.

### Correspondence to:

V. Maupin,  
[valerie.maupin@geo.uio.no](mailto:valerie.maupin@geo.uio.no)

### Citation:

Maupin, V., Mauerberger, A., & Tilmann, F. (2022). The radial anisotropy of the continental lithosphere from analysis of Love and Rayleigh wave phase velocities in Fennoscandia. *Journal of Geophysical Research: Solid Earth*, 127, e2022JB024445. <https://doi.org/10.1029/2022JB024445>

Received 23 MAR 2022

Accepted 26 SEP 2022

### Author Contributions:

**Conceptualization:** Valérie Maupin, Alexandra Mauerberger, Frederik Tilmann




**Data curation:** Alexandra Mauerberger

**Formal analysis:** Valérie Maupin

© 2022. The Authors.

This is an open access article under the terms of the [Creative Commons Attribution-NonCommercial-NoDerivs License](https://creativecommons.org/licenses/by-nc-nd/4.0/), which permits use and distribution in any medium, provided the original work is properly cited, the use is non-commercial and no modifications or adaptations are made.

# The Radial Anisotropy of the Continental Lithosphere From Analysis of Love and Rayleigh Wave Phase Velocities in Fennoscandia

Valérie Maupin<sup>1</sup> , Alexandra Mauerberger<sup>2</sup> , and Frederik Tilmann<sup>2,3</sup> 

<sup>1</sup>University of Oslo, CEED, Oslo, Norway, <sup>2</sup>GFZ German Research Center for Geosciences, Potsdam, Germany, <sup>3</sup>Freie Universität Berlin, Berlin, Germany

**Abstract** Radial anisotropy (RA) in the upper mantle of the Fennoscandian Shield is analyzed by joint inversion of Love and Rayleigh wave phase velocities measured from recordings of teleseismic events at the ScanArray network. The phase velocities are measured by beamforming using three geographical subsets of the network as well as the full network. We analyze how different procedures for determining the phase velocities influence the final result and uncertainty. Joint inversion of the phase velocities in the period range 22–100 s reveals the presence of similar RA in the three subregions, with an average  $\xi$  value of about 1.05 in the subcrustal lithosphere down to at least 200 km depth. This corresponds to SH waves faster than SV by 2%–3%, a value very similar to those found in other continental regions. Considering this anisotropy together with other observables pertaining to seismic anisotropy in the area, we cannot propose a unique model satisfying all data. We can show, however, in which conditions different types of olivine crystallographic preferred orientations (CPOs) commonly observed in natural samples are compatible with the observations. CPO types associated with the preferred orientation of the *a*-axis, in particular the common A-type CPO, require *a*-axes dipping not more than 25° from the horizontal plane to explain our observations. AG-type CPO, characterized by preferred orientation of the *b*-axis and occurring in particular in compressional settings, can be considered as an interesting alternative interpretation of continental lithospheric anisotropy, provided the olivine *b*-axis is dipping by at least 60°.

**Plain Language Summary** Large earthquakes generate seismic waves which travel all over the globe. Two types of waves, called surface waves, travel along the Earth's surface with varying penetration depths and enable us to study the Earth's structure at depth. Using waves generated by distant earthquakes, we have analyzed the velocity of these two types of surface waves when they travel across a 1,500 × 600 km<sup>2</sup> network of seismological stations located across Sweden, Norway, and Finland, in a geologically old tectonic province called the Fennoscandian Shield. We observe a discrepancy between the velocities of these two types of surface waves and analyze the possible causes for this discrepancy. We conclude that seismic anisotropy of the upper mantle from about 50 to at least 200 km depth is the most likely explanation for our observations. Seismic anisotropy in the upper mantle can be generated by preferred orientation of olivine crystals, a major component of the mantle, due shear flow or compression in a preferred direction. The anisotropy we infer is analogous to what has been found in similar continental regions worldwide, and adds to research showing that, due to long and complex tectonic history, the continental regions are more difficult to decipher than the younger oceanic ones.

## 1. Introduction

Seismic anisotropy arises from the structural or mineralogical fabric and is thus a useful proxy for mapping deformation. In the upper mantle, it is commonly explained by crystallographic preferred orientation of the olivine crystals (e.g., Karato et al., 2008). Earth's zero-order anisotropy component is its radial anisotropy (RA), also called vertical transverse isotropy. It is present in particular in the upper mantle of the PREM model (Dziewonski & Anderson, 1981), where the horizontally polarized S waves (SH) down to 200 km depth have a velocity higher than the vertically polarized S waves (SV) by 2.5% on average. The conventional explanation for this so-called positive RA is the dominantly horizontal direction of the flow in the upper part of the mantle, leading to horizontal preferred orientation of the olivine crystal *a*-axis, which, if averaged in azimuth, results in SH waves faster than SV waves (see review in Maupin & Park, 2015). The sparser regions with negative RA (and thus vertical *a*-axis

**Methodology:** Valérie Maupin, Alexandra Mauerberger, Frederik Tilmann

**Software:** Valérie Maupin, Alexandra Mauerberger

**Validation:** Valérie Maupin, Alexandra Mauerberger

**Visualization:** Valérie Maupin

**Writing – original draft:** Valérie Maupin

**Writing – review & editing:** Valérie Maupin, Alexandra Mauerberger, Frederik Tilmann

orientation) are conversely usually interpreted as indicative of vertical flow. This property has been used to map upper mantle flow directions starting with Nataf et al. (1984). Although this model makes a lot of sense in oceanic domains where large-scale olivine orientation in the upper mantle flow can explain rather well the observed RA (Becker et al., 2008), and where the horizontal flow also yields azimuthal anisotropy (e.g., Schaeffer et al., 2016; Tanimoto & Anderson, 1985), it is less clear how to interpret RA in continental regions, especially those where a complex tectonic history is likely to have reorganized the preferred crystal orientation either passively by large scale tilting of anisotropic blocks, or actively by resetting fast axis directions through ongoing deformation.

RA of the upper mantle is, however, clearly not mainly an oceanic feature. In global studies, positive RA is imaged both in the oceanic and continental lithosphere (Auer et al., 2014; Beghein et al., 2006; French & Romanowicz, 2014; Lavoué et al., 2021; Lekic & Romanowicz, 2011; Moulik & Ekström, 2014; Nettles & Dziewonski, 2008). As opposed to the isotropic S-wave velocity maps of the upper mantle where a general consensus has been reached at large scale, major differences still exist in the RA maps produced by different authors with regard to both the lateral and depth distribution of RA.

RA is also detected at smaller regional scale in continental regions. Early studies (Maupin & Cara, 1992; Wielandt et al., 1987) observed that Love wave phase velocities were too high compared to predictions based on Rayleigh wave velocities and argued that this so-called Love-Rayleigh discrepancy could be explained by RA. This was later on confirmed by similar observations in many different regional studies (e.g., Calo et al., 2016; Freybourger et al., 2001; Gaherty, 2004; Lebedev et al., 2009; Pedersen et al., 2006; Ravenna et al., 2018).

The ubiquitous nature of the RA derived from surface wave phase velocity studies, its much poorer correlation with tectonic setting compared to isotropic velocity variations, and the difficulties in interpreting it jointly with azimuthal anisotropy pose the question of its origin. Early studies considered the possible interference with overtones (e.g., Maupin & Cara, 1992). Although it has been convincingly argued that overtones interference is not able to explain the RA at global scale (Laske & Widmer-Schmidrig, 2015; Nettles & Dziewonski, 2011), more recent results show that biases at smaller geographical scale cannot be excluded (Foster et al., 2014; Hariharan et al., 2022). One may also question the role of lateral heterogeneities. It is well established that local phase velocities can be biased by the presence of local lateral heterogeneities and by interfering wavetrains (Kolínský et al., 2021; Wielandt, 1993).

In addition, the anisotropy seen by long-wavelength seismic waves arises from a nonlinear superposition of intrinsic anisotropy and small-scale heterogeneities. This issue, introduced for fine-layered structures in Backus (1962), has been addressed much more generally in recent years (Alder et al., 2017; Magali et al., 2021; Wang et al., 2013), and the question of possible biases related to heterogeneities can be better quantified today.

In the present study, we investigate the possible presence of RA in the old continental lithosphere of Fennoscandia by measuring and jointly analyzing the phase velocities of Love and Rayleigh waves generated by teleseismic events, paying special attention to possible biases in the measurements. We use data from a recent relatively dense seismological deployment covering most of the Fennoscandian Shield, a region situated on the western side of the East European Craton. The Rayleigh wave phase velocities from the same data set have been analyzed by Mauerberger et al. (2021, hereafter Paper I) and Mauerberger et al. (2022, hereafter Paper II) and we refer to these papers for a more detailed description of the tectonic history of the study region. We just note here that the Fennoscandian Shield formed in the Precambrian by progressive amalgamation of several provinces from north-east to southwest, from a 3.3 Ga old terrane in the north to a 0.9 Ga old one in Southwestern Scandinavia. The western flank of the Shield was affected by the Caledonian orogeny (mostly 430–410 Ma) and major Permian rifting (295–275 Ma) reworked its southern edge. It represents a quite typical old continental region with a complex tectonic history. The thickness of the thermal lithosphere in our study region is estimated to vary between 125 and 225 km (Artemieva, 2019). Positive RA has already been found by analysis of Rayleigh and Love waves phase velocities in two studies neighboring our study region to the Northeast (Pedersen et al., 2006) and to the Southwest (Köhler et al., 2015). Lithospheric radial and azimuthal anisotropy has also been mapped from P-wave and S-wave residuals (Eken et al., 2008, 2012) and SKS-wave splitting (Eken et al., 2010; Grund & Ritter, 2020).

## 2. Data Selection and Processing

The data basis, selection, and processing used in this study follow very closely the one in Paper I, where Rayleigh waves from the ScanArray network were analyzed by beamforming.

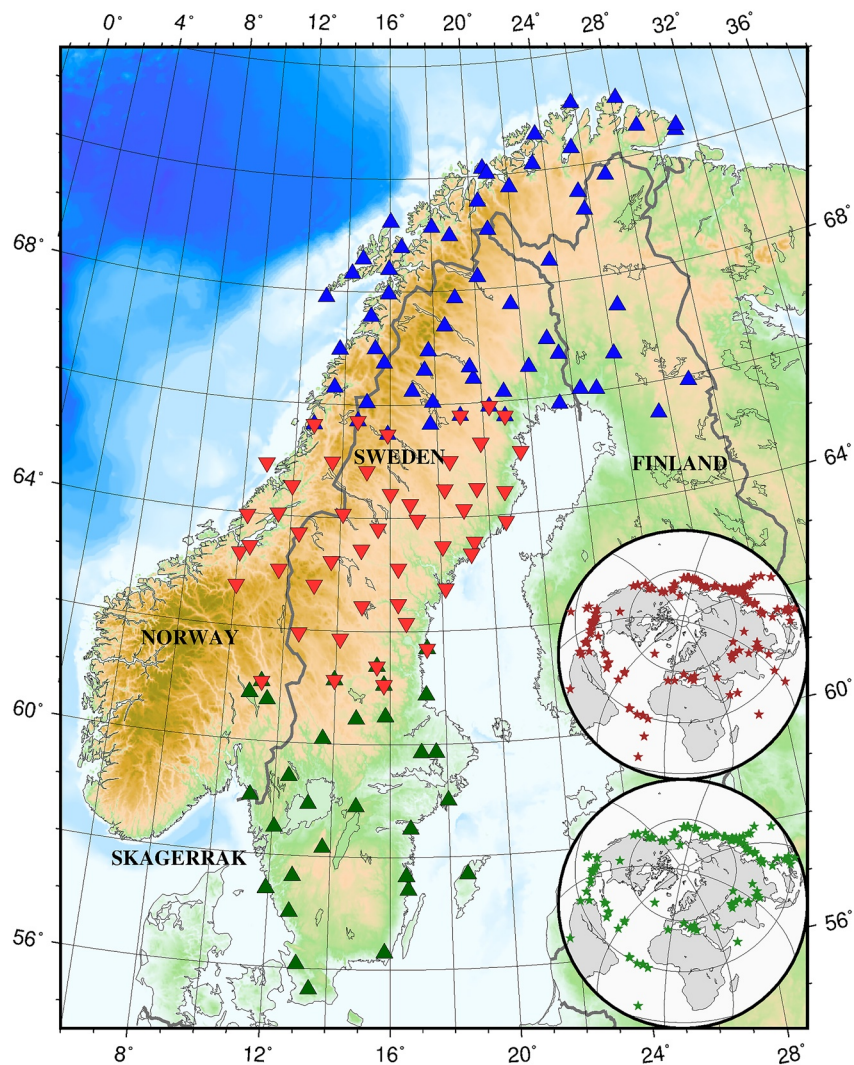


**Figure 1.** Map of the seismic stations in the North (blue), Central (red), and South (green) regions. Note that the subarrays are slightly overlapping, as shown by superposed symbols (superimposed up and down triangles appearing as stars). The insets are centered on the study region and show the distribution of events used for Rayleigh (brown) and Love waves (green) at 40 s period with the total network.

The ScanArray data set is a collection of seismic data from Fennoscandia following the temporary deployment of stations from 2012 to 2017 (Thybo et al., 2021), which we supplement with stations from several permanent networks (Figure 1). We select only a subset of the ScanArray stations to ensure a regular coverage. The full network is divided into three different subarrays covering the North, Central, and South parts of the Scanarray deployment with 62, 48, and 31 stations, respectively (Figure 1 and complete list in the Supporting Information). This division is not geologically based. It aims at building subarrays as large as possible to maximize the resolution in phase velocity, yet having similar dimensions in different directions to ensure a rather uniform resolution with azimuth. Events with magnitude larger than 5.6, depth smaller than 150 km, and epicentral distances from 20° to 120° were selected for analysis, resulting in the event distribution shown in the insets of Figure 1 (number of events per period and complete list in Figures S2 and S3 in Supporting Information S1).

The phase velocities of the Love and Rayleigh wave fundamental modes are measured following the same data rejection criteria and beamforming procedure as in Paper I, a slightly modified version of the procedure introduced in Maupin (2011). The procedure is shortly summarized below and illustrated with a data example (Figure 2).

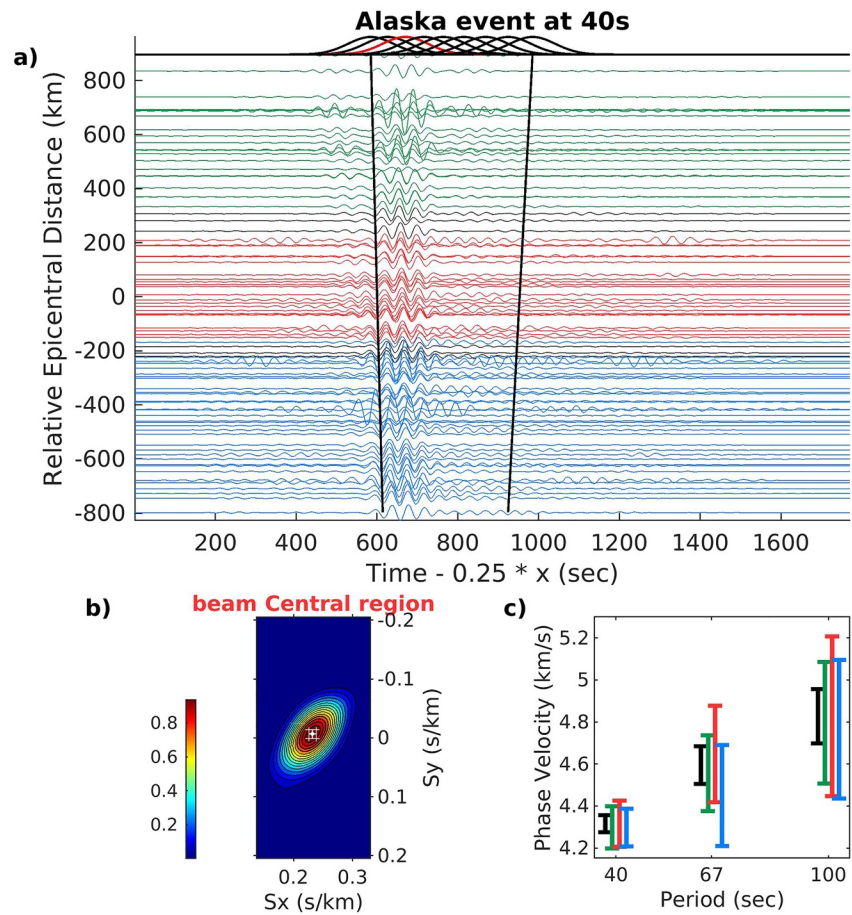


**Figure 2.** Data and beamforming example for an event in Alaska on 2015/05/29 at 73 km depth. Plot (a) shows the normalized transverse components filtered at 40 s period that have passed the selection criteria. The traces are ordered by epicentral distance with respect to a reference point in the center of the network and are colored according to the subarray they belong to (North: blue, Central: red, South: green, black if belonging to two subarrays). The Gaussian functions used to window the data are shown at the top. They are centered on different group velocities with the two extreme velocities denoted by the two straight black lines across the traces. The window for which the beam has maximum amplitude is shown in red. Plot (b) shows the beam power normalized to its maximum value as a function of slowness for the traces belonging to the Central subarray windowed by the red Gaussian window. The white cross shows the width at 98% of the maximum amplitude, selected to define error bars on the phase velocity. Plot (c) shows the phase velocity measured at periods of 40, 67, and 100 s for the three subarrays (same color code as plot (a)) and the full network (black) and their error bars.

Data are extracted in time windows, called “Full window” in the next sections, chosen to cover the whole range of possible group velocities in the frequency range of interest, from 2.7 to 4.5 km/s for Rayleigh waves and from 3.0 to 4.6 km/s for Love waves, and extended on both sides by tapering windows of 500 s. It is clear that unwanted signals like coda waves and overtones may arrive in this time window. As long as the array dimension is such that the phase velocity of the fundamental mode and the overtones can be distinguished as individual peaks by the beamforming procedure, and that only data with a dominant fundamental mode are selected, this does not need to be a problem. We have however chosen to refine the procedure to further reduce the risk of contamination by overtones.

The additional step in the processing consists of multiplying the data by period-dependent moving Gaussian windows centered at a selection of period-dependent group velocities (Figure 2a). We then apply beamforming on these differently windowed data, and select the phase velocity of the beam with the largest energy among the different windowed data. This procedure is similar to the classical one used for single-station phase velocity measurement, where a group-velocity analysis is performed before measuring the phase of the signal at the location of the maximum energy in the frequency-group velocity plane (Levshin et al., 1972). We used Gaussian

**Table 1**  
Butterworth Filters Used for This Study

Period(s)	Corner frequencies (Hz)
100.	0.005–0.015
67.	0.010–0.020
40.	0.020–0.030
29.	0.030–0.040
22.	0.040–0.050

windows with a half-amplitude width of  $3.3 T$ , where  $T$  is the period of interest, as recommended by Wielandt and Schenk (1983) to optimize the trade-off between time and frequency resolution.

The beamforming is performed at five periods, ranging from 22 to 100 s, chosen in such a way that the measurements can be considered as independent. The signals are bandpassed with Butterworth filters with frequency ranges in Table 1.

The major steps of the beamforming procedure are illustrated in Figure 2 for Love waves generated by an event located in Alaska, with backazimuth  $355^\circ$ . The 40 s bandpassed data that have passed the selection criteria are plotted in Figure 2a in a time-distance plot. Beamforming is performed by computing the cross-power spectra of the phase-shifted seismograms for a series of slowness vectors  $\vec{s}$ :

$$P(\omega, \vec{s}) = \sum_{i,j} a_i \exp(i\phi_i) a_j \exp(-i\phi_j) \exp\left(i\omega \vec{s} \left(\vec{X}_i - \vec{X}_j\right)\right) \quad (1)$$

where  $a_i$ ,  $\phi_i$ ,  $a_j$ , and  $\phi_j$  are the spectral amplitudes and phases at stations  $i$  and  $j$ .  $\vec{X}_i = (x_i, y_i)$  and  $\vec{X}_j = (x_j, y_j)$  are the coordinates of stations  $i$  and  $j$  in an event-dependent coordinate system where  $x$  is along the source-station great circle away from the earthquake source and  $y$  follows epicentral-distance dependent small circles to account for the curvature of the wavefronts, an element which is not negligible for the array aperture that we have and the moderate epicentral distances of some events. The resulting beam power as a function of slowness is shown in Figure 2b at 40 s period for the Central subarray. The maximum of the beam power is used to determine the phase velocity and the azimuthal deviation that best characterize the data at the subarray. Phase velocities estimated at the three longest periods of 40, 67, and 100 s for the full network and the three subarrays are shown in Figure 2c. The error bar for each individual phase velocity measurement is determined by using the width of the beam power at 98% of the maximum amplitude. The size of this error bar is rather large and is essentially determined by the dimension of the array. The error bars are not used to weight the different measurements when computing the mean or the median as inspection of many cases has shown that this way of measuring the error does not give a proper measure of its reliability. Processing of the same event at 100 s period and of another event are illustrated in Figures S4–S6 in Supporting Information S1.

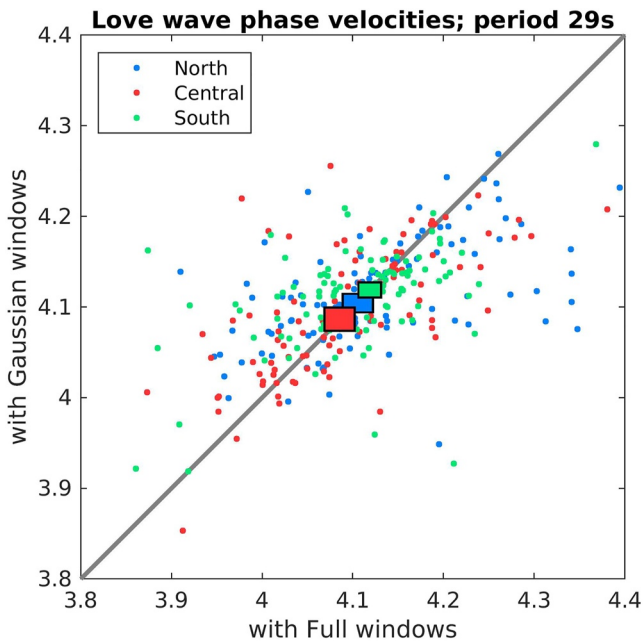


**Figure 3.** Comparison of the Love wave phase velocities measured with Full-time windows and with moving Gaussian windows at 29 s period. The velocities are given in km/s and are shown in different colors for the North, Central, and South regions. A diagonal gray line shows where the two velocities are equal to each other for reference. The colored rectangles show the 95% confidence intervals of the median velocities for each region.

### 3. Phase Velocities

#### 3.1. Full Windows Versus Gaussian Windows

Figure 3 shows a comparison of the Love wave phase velocities measured with the Gaussian window and the Full window procedures in the three regions at 29 s period. There is, of course, some dispersion of the measurements, which partly represents inter-event variability, and partially systematic variations with azimuth (see next section). A systematic bias toward higher or lower velocities would appear as a predominance of data points above or below the diagonal line of the figure. This does not appear to be the case, as confirmed by the fact that the median values plot along the diagonal line. There is less dispersion along the vertical axis than along the horizontal axis, suggesting that moving Gaussian windowing tends to remove noise in the measurements. There is also less dispersion for the South subarray compared to the North and Central regions. The reduced dispersion is also seen when computing the standard deviation of the median, which is about 50% smaller for the Gaussian windows than for the Full windows. We can also notice the large overlap between values measured in the different regions, suggesting no

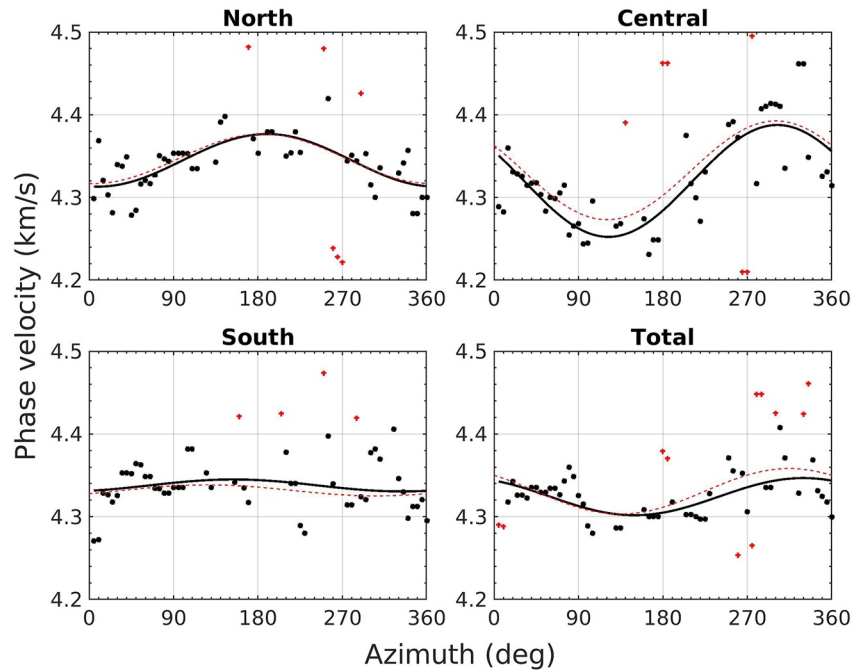


**Figure 4.** Azimuthal variation of the azimuthally binned phase velocities and their  $2\pi$ -periodic fit for Love waves at 40 s period in the three regions and with the total network. The black line denotes the final fit to the black data points. The red dashed line shows the original fit to the data including outliers in red, defined as points with a misfit larger than 1.25 times the standard deviation of the residuals relative to the original fit. Two outliers at high velocities are omitted from the figure in the Central region, and three at low values in the South region, to optimize the vertical scale.

large heterogeneity in the study region. This similarity between the regions is actually reinforced by the Gaussian windows procedure.

These remarks are also valid for the Rayleigh waves. We also checked that the group velocities corresponding to maximum energy are changing with period and backazimuth as expected, and very similarly for the three regions. For example, at shorter periods, the group velocities are larger for dominantly oceanic paths to the West and lower for continental paths to the East.

### 3.2. Azimuthal Variations

An unusual  $2\pi$ -periodic azimuthal variation of the Rayleigh wave phase velocities was observed in the North and South regions in Paper I, and was interpreted as resulting from the proximity of a rather abrupt lateral variation of the lithosphere. We revisit this variation to verify the influence of the slightly modified beamforming procedure, and we complete it with the analysis of the azimuthal variation of the Love waves phase velocities. The combination of azimuthal variation and uneven azimuthal distribution of the events may introduce biases in the evaluation of the mean or median phase velocity and the azimuthal variation. To reduce such biases, we group the measured phase velocities in  $10^\circ$  wide backazimuth bins, with an overlap of  $5^\circ$  between the bins, and compute the median in each bin. The phase velocity used for further depth inversion in Section 4 is the median of these median phase velocities. Both binned and unbinned phase velocities are used to examine the  $2\pi$ - and  $\pi$ -periodic azimuthal variation of the phase velocities with the same procedure as in Paper I. We show here only the results using binned velocities. The results before binning are rather similar, although more dispersed.

Figures 4 and 5 show the azimuthal variation for Love waves at 40 and 100 s periods and Figure S9 in Supporting Information S1 summarizes the amplitude of the variation at all periods. As the Love waves are generally more noisy than the Rayleigh waves, the binning in  $10^\circ$  intervals is quite essential in this case to be able to extract the azimuthal variation with confidence. We observe some  $2\pi$ -periodic variation for all regions. The amplitude increases with period from 0.5% to 2.5% except in the Central region, where a larger amplitude of 1.5% is

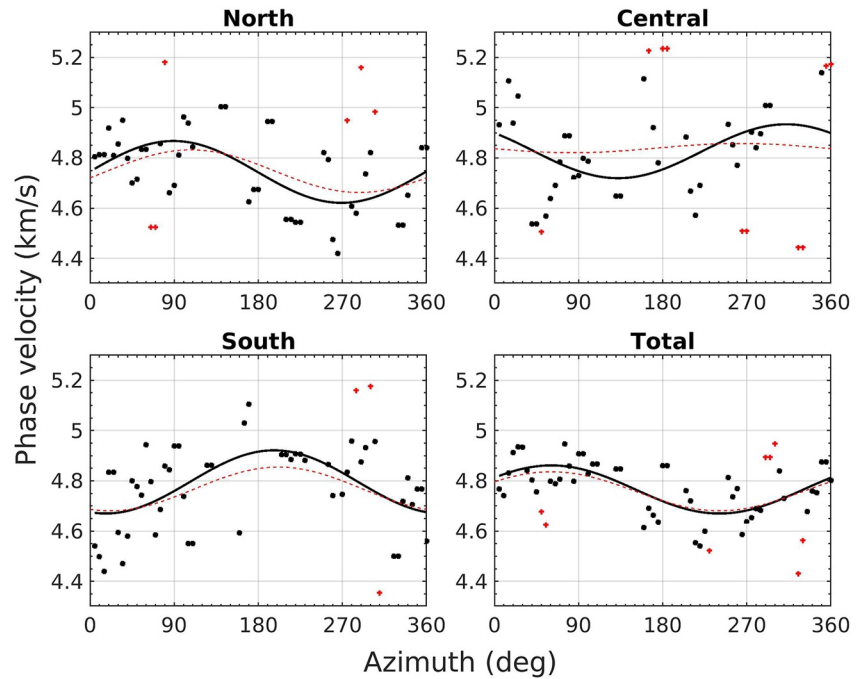


**Figure 5.** The same as Figure 4 at 100 s period. Two outliers at low velocities are omitted in the North region, one at high velocity in the Central region, and two at low values in the South region, to optimize the vertical scale.

observed at the shortest periods. We cannot resolve any significant  $\pi$ -periodic variation, nor the  $\frac{\pi}{2}$ -periodic variation expected for Love waves in anisotropic structures (Maupin & Park, 2015).

The azimuthal variation of the phase velocity for Rayleigh waves in the three regions as well as for the full network is shown at 40 s period in Figure S7 in Supporting Information S1 and summarized in Figure S8 in Supporting Information S1. We notice a clear  $2\pi$  component in the North with an amplitude of about 2% of the phase velocity, in good agreement with Paper I. Numerical modeling in Paper I shows that the proximity of a major lithospheric step is likely responsible for this variation. A smaller but still significant azimuthal variation is observed in the Central region at short periods of 22 and 29 s, but the variation in the South is not significant, in contradiction with Paper I. As in Paper I, we do not resolve any significant  $\pi$ -periodic variation, as would be expected in weakly anisotropic media (Smith & Dahlen, 1973).

It is beyond the scope of the current work to analyze the significance of this azimuthal variation, but we can notice that the maximum velocity for Love waves in the North is not in the same azimuth as for Rayleigh waves. The Love waves in the Central region show a very large azimuthal variation, but the regression has eliminated a rather large number of outliers in this case. We can also note on these figures that the azimuthal variation clearly dominates the regional variation.

### 3.3. Evaluation of the Phase Velocity and Its Uncertainty

The phase velocities selected for depth inversion are those computed as the median of the phase velocities computed with moving Gaussian windows after azimuthal binning. To evaluate the 95% confidence interval of this median, we used an interval of  $\pm$  twice the standard deviation  $\sigma$  of the median computed as (Menzel, 1961):

$$\sigma = \frac{1.2\sigma_M}{\sqrt{n}} \quad (2)$$

where  $n$  is the number of observations and  $\sigma_M$  is their mean average deviation (MAD).

To ensure that this interval corresponds to a realistic value of the uncertainty in our evaluation of the phase velocity, we verify that different ways of measuring the velocity yield values that fall within this interval. We

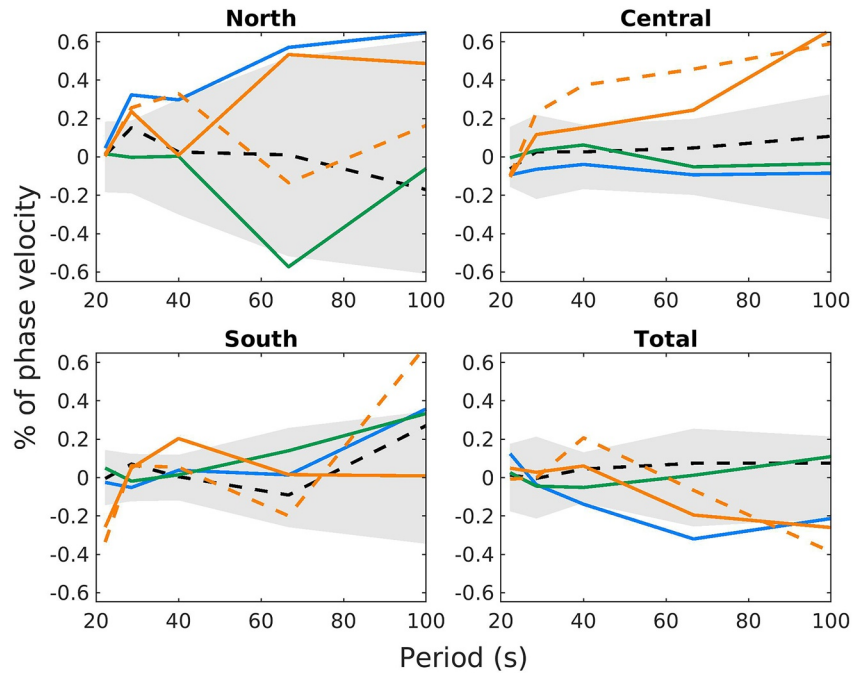


**Figure 6.** Difference as a function of period between the Rayleigh wave phase velocities measured by different methods and the median velocity after azimuthal binning of the velocities measured with Gaussian windows, with its 95% confidence interval shown as a gray area. Black dashed lines: median of the phase velocities measured with Gaussian windows without azimuthal binning. Orange lines: median with Full windows without (dashed) and with azimuthal binning (full). Green lines: average velocities after regression analysis of the Gaussian window binned velocities to analyze the  $2\pi$ -periodic variation. Blue lines: the same for the  $\pi$ -periodic variation.

compare the velocities computed with Gaussian or Full-time windows, before and after azimuthal binning, and the constant terms obtained by the fit to  $2\pi$ -periodic and  $\pi$ -periodic variations. Figures 6 and 7 show, respectively, for Rayleigh and Love waves, the difference between these velocities and the one selected for inversion, the median of the binned velocities measured on Gaussian windows, together with the 95% confidence interval of this median.

We observe that the different curves generally fall within or close to the confidence interval, except for the unbinned data of the Rayleigh waves with full window in the Central region. This is actually more related to a small confidence interval than to a large difference between the velocities. The Rayleigh waves have a larger confidence interval in the North, probably related to the dispersion of the velocities due to the azimuthal variation. The Love waves have confidence intervals two to three times larger than the Rayleigh waves, and more clearly increasing with period. The confidence interval is smaller for the total network than for the regional results, reflecting that the larger number of data is not offset by the dispersion that would have occurred in a more heterogeneous region. Furthermore, the Rayleigh wave tomography (in Paper II) showed that the variation in East-West direction appears to be more significant than the variation in North-South direction, implying that any existing regional variations will affect the subarrays and total network similarly.

Figure 8 shows the phase velocities in the three regions and in the total network together with the confidence intervals in the Central region. These curves attest to the rather homogeneous nature of the region at large scale. The phase velocities in the total network are measured to verify the influence of the size of the network on the phase velocities. It is well-established that phase velocities measured with phase differences only do not necessarily correspond to the structural phase velocity we need for structural interpretation (Wielandt, 1993), due to the influence of lateral amplitude variations when the wavefield is complex. For example, Kolínský et al. (2021) have shown with data from the dense AlpArray network that phase velocities measured with small arrays may be significantly influenced by interference of several wavetrains. Although the variations will vary for waves coming from different directions, we do not know if averaging over several directions leaves a bias with respect to the structural phase velocity, and if this bias is different for Rayleigh and Love waves. As this might influence



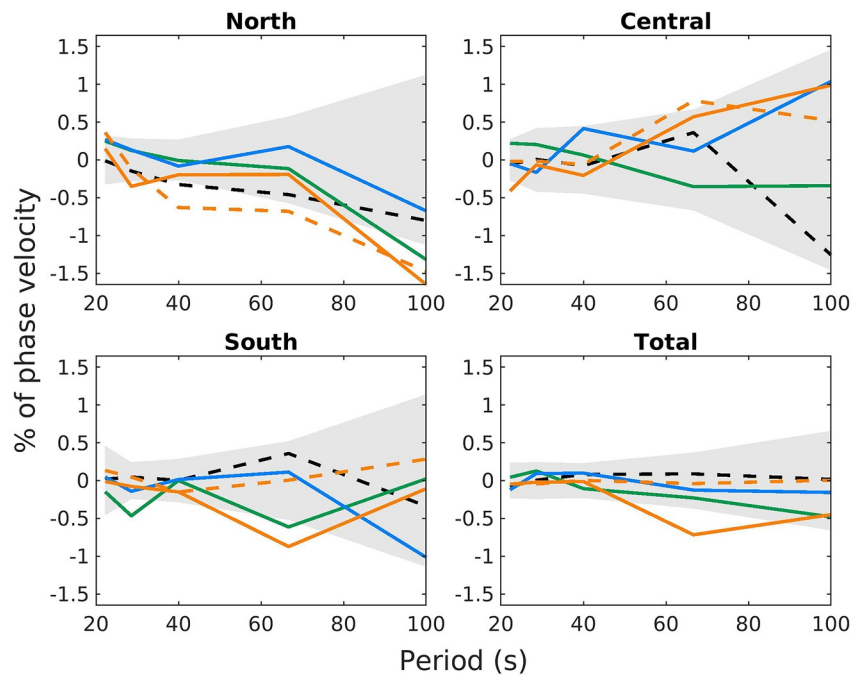


Figure 7. The same as Figure 6 for Love waves.

the Love-Rayleigh discrepancy, and as we expect this possible bias to diminish with network dimensions, we pay special attention to the velocities measured with the total network compared to the three regions. The Rayleigh waves are slightly faster for the total network than for the regional measurements, and the Love waves are slower at the longest periods (Figure 8). These differences, although contributing to a reduction of the Love-Rayleigh discrepancy, are however too small to remove it, as we will see in the next section.

We also compare our results with those of two studies of Rayleigh and Love wave phase velocities in neighboring regions. The velocities denoted “Finland” were measured in southern Finland, to the East of our Central region, in the framework of the SVEKALAPKO experiment (Pedersen et al., 2006). The phase velocities for Rayleigh and Love waves are slightly lower at short periods and higher at long periods than in our case, reflecting the thicker crust and rather high mantle velocity in this area. The phase velocities denoted “Skagerrak” were measured by Köhler et al. (2015) to the West of our South region, partly overlapping. The Rayleigh wave phase velocities reflect the thinner crust and lower mantle velocities. The Love waves phase velocities are particularly high, but also not very well constrained in their study due to the short time interval of data availability.

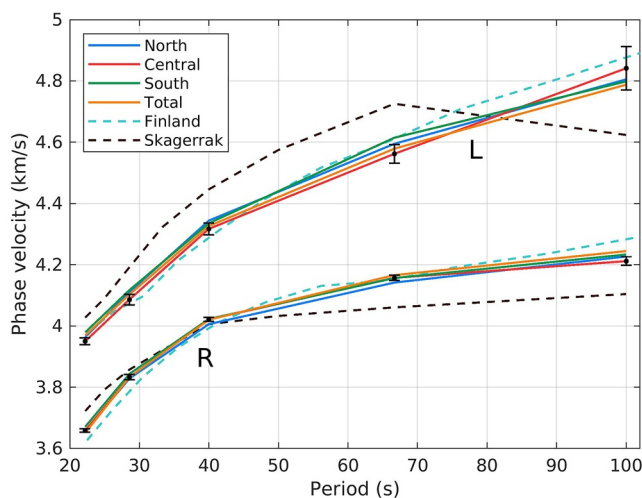


Figure 8. Summary of the phase velocities of the Rayleigh (R) and Love (L) waves measured in the three regions and with the total network. The 95% confidence intervals are shown with black symbols for the Central region only for clarity. The phase velocities measured in the adjacent regions of Finland (Pedersen et al., 2006) and Skagerrak (Köhler et al., 2015) are shown for comparison.

## 4. Depth Inversion

### 4.1. Method and Initial Model

The median phase velocities obtained in the previous section are inverted primarily for different models with depth of perturbations of  $V_{SV}$  and  $\xi = \left(\frac{V_{SH}}{V_{SV}}\right)^2$ , the two elastic parameters with largest influence on Love and Rayleigh wave phase velocities (see, e.g., Maupin & Park, 2015), but we also test the possible influence of variations in P-wave velocity and density.

For mantle structure, the relatively linear relation between phase velocity perturbation  $\delta c$  measured at period  $T_i$  and model parameter perturbations  $\delta V_{SV}$  and  $\delta \xi$  sampled at depth  $z_j$  allows us to use the linearized relation between data and model:

$$\frac{\delta c(T_i)}{c(T_i)} = p_{SV}(T_i, z_j) \frac{\delta V_{SV}(z_j)}{V_{SV}(z_j)} + p_{\xi}(T_i, z_j) \frac{\delta \xi(z_j)}{\xi(z_j)} \quad (3)$$

where the partial derivatives  $p_{SV}(T_i, z_j)$  and  $p_{\xi}(T_i, z_j)$  are displayed for Rayleigh and Love waves in Figure S10 in Supporting Information S1.

The inversion is done using an algorithm first described in L ev eque et al. (1991) and first used for joint inversion of Love and Rayleigh waves in Maupin and Cara (1992). The specificity of this algorithm is to parametrize the model as an arbitrary continuous function with depth, with discontinuities in the parameters introduced only at physical interfaces. In the present case, the model has two interfaces: a mid-crustal one and a crust-mantle interface, defining the upper crust, lower crust, and mantle as the three layers of the model. The discretization is done by sampling the function at different depths.

As the model parameters are parametrized as a continuous function with depth sampled at different points, we need to ensure that the inversion does not depend on the sampling, which has to be tighter than the depth resolution of the inversion. This is achieved by introducing a correlation function that controls the smoothness of the model variations with depth in each layer by partly coupling the variations of the parameters at neighboring points through nondiagonal terms in the model a priori covariance matrix  $C_{mm}$ . We use Gaussian correlation functions and vary the correlation length with depth.  $C_{mm}$  between the model parameters at two depth-points  $z_1$  and  $z_2$  is expressed as:

$$C_{mm}(m(z_1), m(z_2)) = \begin{cases} \sigma_m^2 \exp\left(-\frac{(z_1 - z_2)^2}{2L(z_M)^2}\right) & \text{for } z_1 \text{ and } z_2 \text{ in the same layer} \\ 0 & \text{otherwise} \end{cases} \quad (4)$$

where the correlation length  $L$  is a chosen function of  $z_M$ , the mid-point between  $z_1$  and  $z_2$ , and  $\sigma_m$  is the a priori standard deviation of the model parameters. Most inversions are done here with a correlation length varying linearly with depth from 20 km at the surface to 100 km at 400 km depth, but other values are also tested. The variations are decoupled across the interfaces.

The efficiency of the inversion is related to the rather linear relation between variations in model parameters and surface waves phase velocities. It is based on the fundamental formula for linear inversion (Tarantola & Valette, 1982):

$$\vec{m} - \vec{m}_0 = (G^T C_{dd}^{-1} G + C_{mm}^{-1})^{-1} G^T C_{dd}^{-1} (\vec{d} - \vec{d}_0) \quad (5)$$

where  $\vec{m}$  is the inverted model,  $\vec{m}_0$  is the a priori model, also used as starting model,  $\vec{d}$  are the measured phase velocities and  $C_{dd}$  their covariance matrix (based on data uncertainty presented in the previous section);  $C_{mm}$  is the model a priori covariance matrix. One may notice in Equation 5 that in this formulation the ratio between  $C_{mm}^{-1}$  and  $C_{dd}^{-1}$  plays the role of the damping parameter introduced in other formulations. In the present case, we keep  $C_{dd}$  fixed to the values given by the data errors and use different values of  $C_{mm}$  to effectively vary the damping and/or weight the importance of the different parameters used in the inversion. Both  $\vec{d}_0$ , the phase velocities in the initial model, and  $G$ , the matrix of partial derivatives  $p(T_i, z_j)$  with respect to the model parameters, are calculated using software from Saito (1988). This software takes into account the Earth's sphericity, a necessity to avoid biases at long periods. The interfaces between layers are kept fixed in our procedure, but, as the model has only two interfaces, we can easily test the influence of their depth on the result.

The upper 120 km of the starting model used in most inversions is taken as an average of the results from Paper II in the area covered by the present study. In that paper, the average Moho depth is found to be at 45 km, in good agreement with the average depth of 44.6 km obtained in the area with receiver functions (Olsson et al., 2008). The S-wave velocity does not show any jump at the mid-crustal interface, only a change in vertical gradient. The insertion of a mid-crustal interface in the initial model allows decoupling between upper and lower crust

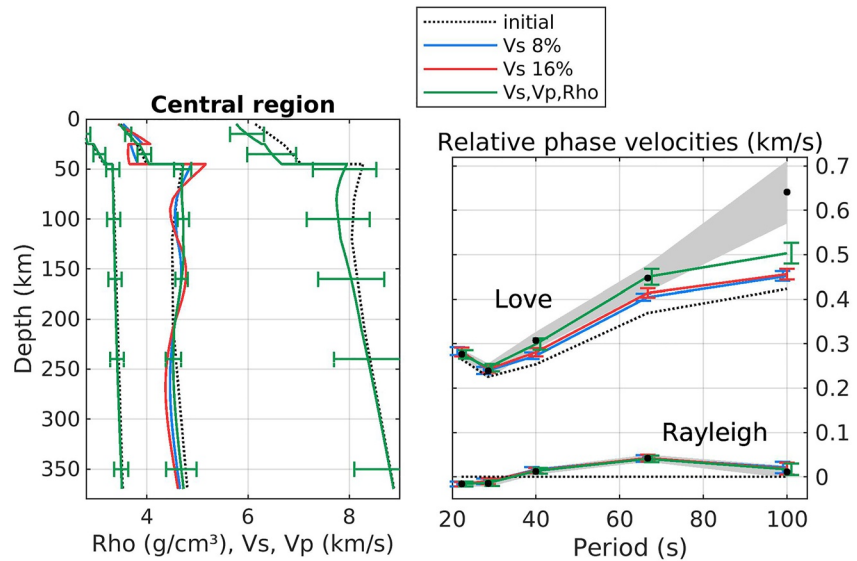


**Figure 9.** Results of selected isotropic inversions of the phase velocities in the Central region. The left panel shows the models with depth from inversions for  $V_s$  only with  $\pm 8\%$  a priori confidence interval (blue),  $V_s$  only with a larger interval of  $\pm 16\%$  (red), and an inversion for density, P-wave, and S-wave velocity (green) with, respectively,  $\pm 4\%$ ,  $\pm 8\%$ , and  $\pm 8\%$  a priori intervals. The initial model is shown as a dotted line. The a posteriori 95% confidence interval is shown at selected depths with a distance between depths corresponding to the correlation length, and only for the last model for clarity. The right panel shows the phase velocity values as a function of period relative to the Rayleigh wave phase velocity in the initial model. The measured phase velocities are shown as black dots with their 95% confidence intervals in gray. The phase velocity in the initial model (dotted black line) and in the inverted models (colored lines) are shown with their respective a posteriori confidence intervals. Note that the colored error bars are plotted at slightly shifted period values to improve visibility.

variations during the inversion and introduction of a jump if preferred by our data.  $V_p/V_s$  is set to 1.76 (Olsson et al., 2008) and the density profile is taken from England and Ebbing (2012). Below 120 km depth, the model is identical to the AK135 model (Kennett et al., 1995). Initial models with other Moho depths and higher mantle velocity are also tested.

As explained above, the damping is regulated by the ratio of the standard deviation of the data and of the a priori model, and we need to take special care in choosing this appropriately. Most of the models shown are produced with a 95% a priori confidence interval (2 standard deviations) equal to 8% for  $V_{SV}$ , but larger and smaller values have also been tested. 8% is a rather generous interval that lets the inversion change the model significantly. The corresponding interval for  $\xi$  is set to 10% (corresponding to 0.1). Considering the factor 2 due to the square in the definition of  $\xi$  with respect to velocities, this is actually a smaller interval for  $\xi$  than for  $V_{SV}$ , and will actually favor velocity variations rather than anisotropy in fitting the data. The influence of P-wave velocity and density variations were also tested, with different degrees of correlation with the variation of the S-wave velocity.

#### 4.2. Isotropic Inversions

Figure 9 summarizes different attempts to jointly invert the Rayleigh and Love wave phase velocities for isotropic models. (This is effectively done by inverting for  $V_{SV}$  and keeping  $\xi = 1$ , thus ensuring  $V_{SH} = V_{SV}$ .) We show only the results for the Central region, as the results obtained in the other regions are very similar. The left panel shows different inverted models and the right panel shows the corresponding phase velocities. Inversions for  $V_s$  only with a 95% a priori confidence interval of  $\pm 8\%$  (blue lines) lead to models which are slightly oscillatory with depth, and with a low-velocity lower crust. Most importantly, these models manage to fit the Rayleigh wave phase velocities in the full period range, but are too slow for the Love wave phase velocities from 40 s period onwards. Decreasing the damping by doubling the a priori confidence interval (red lines) increases the amplitude of the depth oscillations in the model but does not significantly improve the fit. Changing the correlation length with depth influences the amplitude of the oscillations in the model and their wavelength, but does not improve the fit to the data (Figure S11 in Supporting Information S1). The same happens when changing the initial model in the

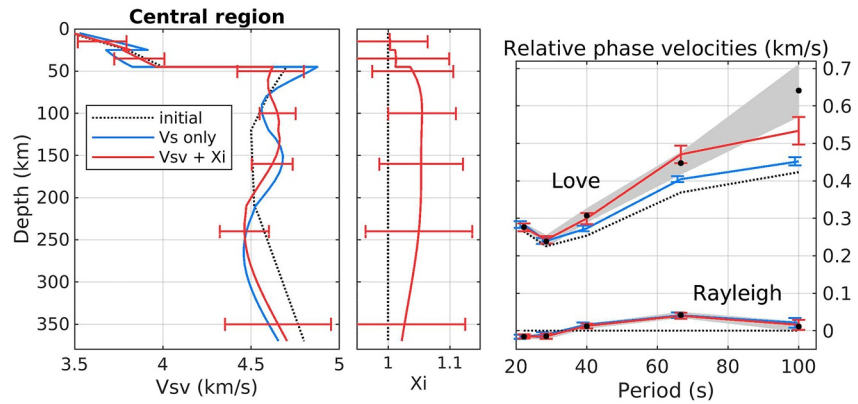


**Figure 10.** The same as Figure 9 but for inversions for  $V_{sv}$  and  $\xi$  (red) in addition to inversion for  $V_s$  only (blue). For clarity, and as they are similar to those for  $V_{sv}$ , the a posteriori confidence intervals of the model are not shown for  $V_s$ . The middle panel shows the variation of  $\xi$  with depth.

mantle (Figure S12 in Supporting Information S1) or when moving the Moho discontinuity to 40 or 50 km depth (Figure S13 in Supporting Information S1).

Adding P-wave velocity and density as inverted parameters without any coupling to  $V_{sv}$ , and with a priori 95% confidence interval of  $\pm 8\%$  for P waves and  $\pm 4\%$  for the density (green lines in Figure 9) does not improve the result either. The fit to the Love wave phase velocities has improved, although it is still outside the confidence interval at the longest periods, but the model is rather unrealistic: the increase in S-wave velocity in the mantle is associated with a significant decrease in P-wave velocity in the crust and in the mantle, where the P-wave velocity is below 8 km/s down to 150 km depth. The density is not much affected in the present case.

In conclusion, we see that realistic isotropic models cannot jointly fit the Rayleigh and Love wave phase velocities in any of the regions we have studied.

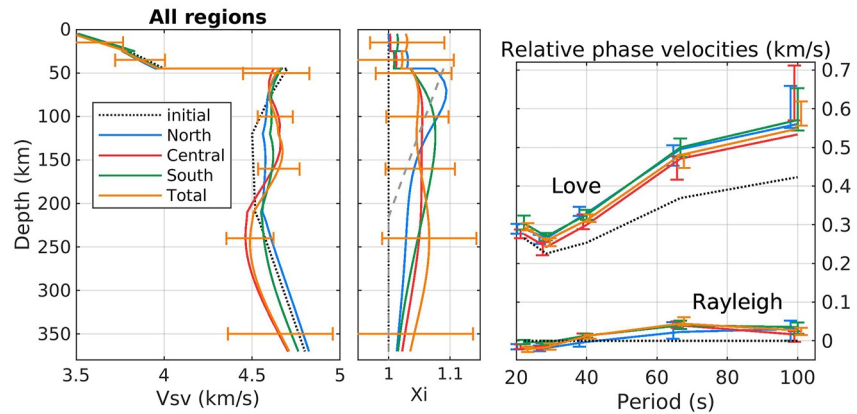
### 4.3. Anisotropic Inversions

Figure 10 shows the result of introducing RA in the model. Note that the velocity shown in the left panel is the SV-wave velocity in this case. Compared with the isotropic case shown in blue, the SV-wave velocity is less oscillatory, and the depth profile is far less dependent on the correlation length (Figure S14 in Supporting Information S1). The value of  $\xi$  is slightly larger than 1 in the crust, but the dominant feature is the positive anisotropy in the mantle, where  $\xi$  reaches a maximum of about 1.05 between 100 and 200 km depth. This so-called positive anisotropy, in reference to the higher than 1 value of  $\xi$ , yields a better fit to both Rayleigh and Love wave dispersion curves, although the longest period of Love waves are still predicted to be somewhat slower than observed (cf., Figure S12 in Supporting Information S1). Introduction of P-wave velocity and density as additional parameters, as well as changing Moho depth (Figure S15 in Supporting Information S1) and the correlation length (Figure S14 in Supporting Information S1) do not alter these conclusions.

The resolution, illustrated at selected mantle depths in Figure S16 in Supporting Information S1, shows that only large-scale (about 100 km) depth variations of the parameters are resolved, but also that there is little trade-off between  $\xi$  and  $V_{sv}$ . The resolution in  $\xi$  is dominantly positive, with only marginal negative excursions with depth, ensuring that the sign of the anisotropy is well resolved.

Figure 11 shows the result of the radial anisotropic inversions in the three regions and for the whole network. The fit to the data is in general very good, except at 100 s for Love waves, where the data are slightly faster than predicted by the models. Let us notice that this long-period misfit is largest in the Central region, and that the predicted phase velocities and data confidence intervals overlap for the three other networks.

The trend in terms of anisotropy is the same in all cases, with a marked positive anisotropy in the mantle. The anisotropy decreases in all cases from 250 km depth, but this depth also corresponds to depths where the resolution of the  $\xi$  parameter starts to fade (cf., Fig. S16 in Supporting Information S1). The anisotropy is deepest



**Figure 11.** The same as Figure 10 but shows the results of anisotropic inversions for the three regions and for the total network. The value of  $\xi$  in the PREM model is shown as dashed gray line in the middle panel. Note that in the right panel, the colored error bars are plotted at slightly shifted period values to improve visibility, and show the estimated 95% confidence intervals of the *measured* phase velocities for the different networks. The solid lines show the corresponding velocities predicted by the inverted models. The a posteriori confidence intervals of the predicted phase velocities are omitted to be able to show the data ones, but they are similar to those shown for the anisotropic inversion shown in Figure 10.

for the whole network, but this is associated with the fact that the Love wave phase velocities have a smaller confidence interval at long periods for this case than in the individual regions. To test the influence of the size of the error bars on the results, we have conducted inversions where, at each period and for each wave, the confidence intervals in the 4 datasets are replaced by the maximum ones obtained in any region. The result is shown in Figure S17 in Supporting Information S1. In that case, the differences between models in different regions originate in their different phase velocity values, and not in differences in uncertainty. The main difference with the case presented in Figure 11 is the decrease in anisotropy at depth for the total network, showing the relation between the depth of the anisotropy and the uncertainty of the long period Love wave phase velocities. There is no major difference in anisotropy for the individual regions, which all had rather large uncertainty intervals in the original datasets, and thereby cannot resolve deep anisotropy. This influence of the uncertainty value also explains why the anisotropy in the total network does not just appear as a simple average of the anisotropy in the three individual regions.

Let us note that the isotropic case  $\xi = 1$  seems to be formally included in the 95% confidence intervals in Figures 10 and 11. The depths at which the error bars are plotted differ in depth by roughly the correlation length and show therefore independent evaluations of the model. The probability of a given model can be estimated by the product of the probability of the model at these different depths. Full isotropy requires excursion of the model to their maximum confidence intervals at three to four independent depths and has therefore a very low probability.

The low probability of full isotropy over the whole depth range can alternatively be seen by using larger correlation lengths. As the inversion is able to resolve large-scale variations better than small-scale ones, the confidence intervals decrease if inversions are performed with larger correlation lengths. To illustrate this, the results for three different choices of correlation lengths are shown in Figure S14 in Supporting Information S1, together with the confidence intervals for the largest correlation length. Isotropy is not included in the confidence interval at 120 km depth in this case. We see that the  $\xi$  models we obtain in all three cases are smooth and similar. This shows the inversion would stand an even larger correlation length and that we can therefore be confident that the positive anisotropy observed in the upper 200 km of the mantle is significant. The SV-wave velocity models are also stable with correlation lengths unlike those resulting from the isotropic inversions (Figure S11 in Supporting Information S1).

We do not discuss here the SV-wave velocity as it is studied in detail in Paper II. We just note that the choice of Moho depth strongly influences lower crust and mantle velocities down to 80 km depth, but not further down in the lithosphere (Figure S15 in Supporting Information S1). The most notable difference between the three regions

is the high-over-low velocity in the lithosphere of the Central region, which corresponds well with the results of Paper II.

## 5. Discussion

The main result of our study is the systematic Love-Rayleigh discrepancy observed at periods longer than 40 s, with Love waves too fast by about 0.07 km/s, and the associated positive RA resolved to at least 200 km depth in the Fennoscandian Shield. Although there are some differences in the depth distribution of the  $\xi$  parameter in the three sub-regions, all models are within each other's confidence intervals, and we will not discuss the differences in anisotropy between the regions. We will rather focus on the possible significance of a general positive RA in an old continental lithosphere. Before going into this discussion, we need to consider if other mechanisms than RA could be responsible for the Love-Rayleigh discrepancy.

### 5.1. Is RA the Only Explanation for the Love-Rayleigh Discrepancy?

The core of our observations is that measured Love and Rayleigh wave phase velocities are incompatible with an isotropic model. The difference in predicted Love wave phase velocities based on the optimal isotropic model and the optimal model with RA is about 0.07 km/s at 67 and 100 s periods (see blue and red phase velocity curves in Figure 10). This means that RA does not explain our observations better than any mechanism that would introduce a bias in the Love wave velocities of 0.07 km/s, or an opposite bias for Rayleigh waves, or a combination of two smaller biases of opposite signs.

Love wave phase velocities, measured on the more-noisy horizontal components, have usually larger error bars than the phase velocities of the Rayleigh waves. The main challenge to detect upper mantle RA confidently is to measure the Love wave phase velocities with sufficient precision, in particular at long periods. Uncertainty and biases may result from interference with overtones, from the effect of lateral heterogeneities, and from long-period noise on the horizontal components.

Although we have refined the beamforming procedure to minimize the effect of undesirable phases on the measurement of the fundamental wave phase velocities, this does not alleviate problems related to interference of the fundamental mode with overtones if they severely overlap in time. Foster et al. (2014) and Hariharan et al. (2022) have analyzed how the interference with overtones affects the phase of the Love wave fundamental mode, and, by derivation, the evaluation of its local phase velocity in a period range and with station configurations relevant to the present study. In the period range 50–100 s, Hariharan et al. (2022) show that the highest fundamental to overtone ratio, and thereby least interference, is achieved for events with depth from 100 to 180 km, but restricting our data to this depth range would reduce the data basis too drastically. Dominantly oceanic paths, where the group velocity of the fundamental mode is high and overlaps with overtones, are shown to be more liable to interference problems. In this study, two main backazimuths correspond to oceanic paths: around 0° for waves having crossed the Arctic Ocean, and around 270° for waves coming from the Atlantic Ocean. Note that the processing examples shown in Figure 2 and Figures S4–S6 in Supporting Information S1 correspond to events in these backazimuths. Except for the high velocities in the Central region at 40 s period, there is no clear correlation between high phase velocities and oceanic paths. At 100 s period in particular, where Love waves are "too fast," the high-velocity values in the full network, with lowest uncertainty, are observed in the northeast quadrant, both for Arctic Ocean paths and purely continental Eurasian paths with lower group velocities. In addition, the direction in which higher velocities is observed varies from region to region, in contradiction to a bias related to unfavorable paths.

Albeit in a smaller period range, overtones interference may also occur for continental paths. Although it introduces first of all dispersion in the measurements but no a priori bias, Foster et al. (2014) note that the interference pattern produces a phase variation with epicentral distance with a saw-toothed pattern that leads to more numerous albeit smaller positive errors in phase velocities than negative ones. This saw-toothed pattern is also clear in the results of Hariharan et al. (2022). Eliminating velocities too far from expected values, but also choosing the median instead of the mean, might therefore introduce a bias toward high velocities. In the present study, at 100 s period, phase velocity values picked by beamforming are accepted between 4.0 and 5.5 km/s, ensuring that we keep the very low-velocity values. At 100 s, the means of the unbinned phase velocity measurements are from 0.02 to 0.036 km/s lower than their corresponding medians for the four different networks. This could therefore hint to a possible bias toward higher values of phase velocities at 100 s, but we note that the difference between

the two values is of the same order of magnitude at other periods, in particular at 67 s period, but with both positive and negative differences depending on network. Examination of events with particularly high or low phase velocity estimations points rather to other causes than overtones interference, like noise or few data at stations with unfavorable geographical distribution. Using the mean instead of the median would have the unfortunate consequence to allow these data to influence the result but would slightly reduce the Love-Rayleigh discrepancy at 100 s period.

Another challenge is the uneven azimuthal distribution of the teleseismic events and the presence of a significant  $2\pi$  azimuthal variation in the phase velocities. We use data binned in azimuthal ranges to reduce the effect of the uneven distribution and we use the variations between different procedures for measurement of the median to estimate the uncertainty, using this to set the phase velocity error for the depth inversion. The presence of the  $2\pi$  variation is however not a simple thing to explain (see Paper I) and we cannot exclude that the median over azimuth does not correspond to the structural mean phase velocity of the Rayleigh and Love waves, in other words that the mechanism that creates the azimuthal variation also creates a systematic bias of the phase velocities toward higher or lower values. If this bias has a different amplitude for Rayleigh and Love waves, it can create a Love-Rayleigh discrepancy unrelated to anisotropy.

The mean-to-peak velocity variation related to the  $2\pi$  variation is in the maximum case 0.06 km/s for Rayleigh waves and 0.07 km/s for Love waves. It is therefore of the same amplitude as the phase velocity “bias” we need for explaining our data. Paper I demonstrates that the  $2\pi$  variation for Rayleigh waves in the North can be explained by the presence of a strong and abrupt lithospheric step on the West side of the network. The azimuthal variation is reproduced by numerical modeling, but one may also notice that the average of the modeled velocities in the two opposite fast and slow propagation directions do not deviate substantially from the structural phase velocities that would be observed in the average 1D structure of the model. According to this modeling, we can therefore infer that the  $2\pi$  variation of the Rayleigh wave phase velocity is not associated with a bias of the median velocity. A similar modeling has not been done for Love waves. It seems, however, unlikely that lateral heterogeneities would bias the Love and Rayleigh waves very differently and create biases of opposite signs.

In addition to the influence of close-by heterogeneities, the wavefield may be influenced by heterogeneities located far away and causing an interference pattern in the phase distribution. Kolínský et al. (2021) show that interfering wavetrains can explain the often wobbly nature of dispersion curves measured with two aligned stations or smaller networks. They show that over a network of 160 km in diameter in the Alps, the variations can attain up to 0.4 km/s. They model waves coming only from one backazimuth but at different locations with respect to the interference pattern, and we assume that this is analog to modeling waves coming from different source directions at one location. The question is if these variations introduce bias in addition to scatter. The interference due to scattering by a low-velocity region, as mainly addressed in that paper, produces negative excursions from the theoretical dispersion curves larger than the positive ones, but occurring in smaller period ranges. How this would combine to bias the median velocities is not easy to infer. Scattering from a high-velocity anomaly creates the opposite pattern, although more symmetric in amplitude than for the low-velocity case. Although this should be checked more quantitatively, there is no indication of a systematic bias of the order of the one needed here in the results of Kolínský et al. (2021). Should however a negative bias be found for Rayleigh waves, but not for Love waves because, for example, of a smaller propensity to scattering, this could partly explain the Love-Rayleigh discrepancy by turning the usual assertion that Love wave velocities are too high to the fact that the measured Rayleigh wave velocities are too low.

The wobbles in the dispersion curves decrease with the size of the network. In the present case, the regional networks are 400–600 km in diameter, thus 2.5–4 times larger than the 160 km subarrays in Kolínský et al. (2021), and the full network is 1,700 km long. As we find the same amount of Love-Rayleigh discrepancy in the different configurations, it seems unlikely that biases due to interfering wavetrains can explain the discrepancy.

We should also consider the effect of small-scale local heterogeneities. Although an early study found the possible contribution of small-scale isotropic heterogeneities to the Love-Rayleigh discrepancy to be very small (Maupin, 2002), it is interesting to revisit this point since much better tools are now available to evaluate the contribution of local heterogeneity to the total anisotropy observed at long wavelength. Generalizing the classical work of Backus (1962), Magali et al. (2021) recently quantified the amplitude of RA resulting from a 2D flow model producing a combination of laterally varying isotropic heterogeneities and crystallographic preferred

orientation (CPO). Both the elongated heterogeneities and the CPO induced by the flow produce positive RA in regions of dominantly horizontal flow. The contribution by lateral isotropic variations with a contrast of 10% results however in artifacts in the  $\xi$  models no larger than 0.02, five times smaller than the CPO contribution. They further found that the Voigt average of the CPO in a given volume is a good first-order estimate of the anisotropy seen by long-wavelength waves. We can thereby infer that small-scale isotropic heterogeneities, in particular horizontally elongated heterogeneities, might contribute to the positive RA observed in the present study, but can hardly explain its full amplitude, whereas CPO yields the right order of magnitude.

## 5.2. Which RA for Different Models of CPO?

Orientation of olivine crystals is the prevailing interpretation of upper mantle anisotropy. The relation between deformation and anisotropy is, however, not unique. As demonstrated by modeling, laboratory experiments, and analysis of natural samples, different conditions in terms of melt, temperature, pressure, and hydration favor different glide systems and lead to several types of CPO, all associated with a different relation between deformation and orientation of the crystallographic axes (reviews by Ben Ismail & Mainprice, 1998; Bernard et al., 2019; Hansen et al., 2021; Tommasi & Vauchez, 2015).

The A-type is the most common CPO type. It orients the *a*-axis in the shear direction and the *b*-axis perpendicularly to the shear plane. Most types of CPO orient the *a*-axis in a given direction, albeit not necessarily in the shear direction (see review by Bernard et al., 2019). Among the non-A CPO types, the B-type has been given the most attention as it orients the olivine *a*-axis in the shear plane but perpendicularly to the shear direction, and thereby leads to erroneous geodynamical models if anisotropy is interpreted in the framework of the classical A-type CPO (Karato et al., 2008). Analysis of natural samples of peridotite shows that different CPO types usually cohabit and that the classical A-type may not dominate by more than 50% in natural samples (Bernard et al., 2019).

To know which CPO type is active is of course crucial to interpret geodynamically the observed seismic anisotropy. From a purely seismological point of view, the anisotropy may however be described irrespective of which type of CPO it is associated with. Most CPO types orient the fast *a*-axis in a given direction in space. Since the anisotropy between the olivine *b*-axis and *c*-axis in the plane perpendicular to the *a*-axis is not strong, most CPO types are in practice equivalent to a quasi-hexagonal or transverse isotropic system with a fast axis of cylindrical symmetry. In these cases, the important parameter from a purely seismological point of view is just the direction of the *a*-axis in space.

An exception to this is the AG-type CPO, also called “a-c switch,” which has been demonstrated experimentally and is commonly observed in natural samples (Ave Lallemand & Carter, 1970; Bernard et al., 2019; Nicolas et al., 1973). It has been associated with weak anisotropy and the presence of melt at mid-oceanic ridges (Hansen et al., 2016) and, importantly for continental settings, also arises in compression at temperature corresponding to the upper part of the subcrustal lithosphere (Demouchy et al., 2014). In this CPO, the *b*-axis orients perpendicularly to the compression direction and the *a*-axis and *c*-axis form a girdle in the perpendicular plane. Since the velocity along the *b*-axis is smaller than the average velocity in the plane formed by the *a*-axis and *c*-axis, this leads to a transverse isotropic system with a slow axis of cylindrical symmetry.

We analyze in Figure 12 the RA expected for these two types of models where either the direction of the *a*-axis, or the direction of the *b*-axis is the important parameter. In analogy with the notation used in P-wave residual studies (Plomerová et al., 2011), we call these A-models and B-models.

More precisely, the *a*-axis of the olivine in our A-models is aligned N-S (in azimuth 0°), dipping from the horizontal plane by 0°–90° (Figure 12a). The *c*-axis is kept horizontal with azimuth 90° (E-W) and the *b*-axis moves from vertical to horizontal, also with azimuth 0°, following the dip of the *a*-axis. These models simulate structures that have acquired their anisotropy as A-type in a horizontally oriented flow and which have subsequently been tilted. They are however also suitable to represent the anisotropy acquired with non-A type CPOs which preferentially orient the *a*-axis in a given direction.

The *b*-axis of the olivine within our B-models is also N-S (in azimuth 0°), dipping from the horizontal plane by 0°–90°, the *a*-axis and *c*-axis forming a girdle in the perpendicular plane. These models simulate orientation by compression reflecting AG-type CPO.



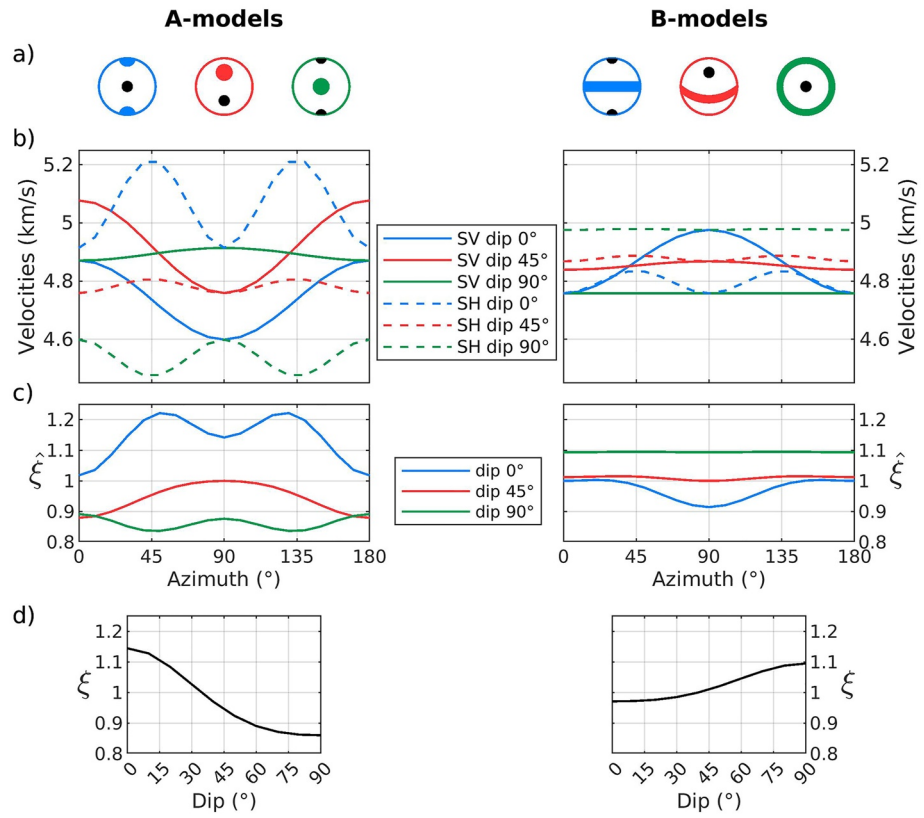


**Figure 12.** Predicted RA for different orientations of pyrolite. Left plots are for A-models and right plots are for B-models. Blue, red, and green colors are used to distinguish cases with 0°, 45°, and 90° dip from the horizontal plane of the *a*-axes or *b*-axes, respectively. The orientation of the olivine crystals is illustrated with schematic pole figures of the lower hemisphere showing the *a*-axis or the (*a*-*c*) girdle in color and the *b*-axis in black. For A-models, the olivine *a*-axis is oriented in azimuth 0° and different dips. The same for the *b*-axis for B-models. The upper plots show the velocity of horizontally propagating long-period SV and SH waves as a function of azimuth for *a*-axis or *b*-axis dipping at 0°, 45°, and 90° from the horizontal plane. The middle plots show the corresponding value of the direction-dependent apparent  $\xi$ . The lower plots show the expected value of  $\xi$  for waves averaged over all azimuths as a function of the dip of the *a*-axis or *b*-axis.

We use the elastic coefficients for pyrolite from Estey and Douglas (1986) and assume the full orientation of the mineral constituents. Using pyrolite with 59% olivine, 17% orthopyroxene, 12% clinopyroxene, and 12% garnet have the advantage of accounting for the presence of other minerals than olivine and their orientation relative to the olivine in the total anisotropy. The anisotropy is, however, dominated by the orientation of the olivine crystals, for which updated measurements of elastic coefficients (e.g., Zhang et al., 2018) are not, for our purpose, significantly different from those in Estey and Douglas (1986).

Figure 12b shows the velocity of horizontally propagating long-period SH and SV waves as a function of propagation azimuth  $\theta$  in models with three different dips of the *a*-axis or *b*-axis. Let us note that S waves in general anisotropic media are split into fast and slow waves which are generally not polarized as SV and SH. In the assumption of weak anisotropy and for waves with period much larger than their splitting time, it is, however, possible to show that the propagation-direction-dependent elastic coefficients  $\hat{L} = L + G_C \cos 2\theta + G_S \sin 2\theta$  and  $\hat{N} = N - C_C \cos 4\theta - C_S \sin 4\theta$  control the velocities of horizontally propagating S-waves with initial polarisation, respectively, SV and SH (Lévesque et al., 1998). These two coefficients are also the main parameters controlling, respectively, the phase velocities of Rayleigh and Love waves (Montagner & Nataf, 1986). Using these velocities instead of Rayleigh and Love phase velocities enables us to present a more general result independent of frequency and of depth distribution of the anisotropy. The resulting direction-dependent apparent  $\hat{\xi} = \frac{\hat{L}}{\hat{N}}$  (Figure 12c) controls the Love-Rayleigh discrepancy for propagation in azimuth  $\theta$ .

We observe that SH waves have higher velocities than SV waves for A-models with no dip of the  $a$ -axis, leading to  $\hat{\xi} > 1$  for all azimuths, in agreement with common understanding. For 45° dip and vertical  $a$ -axis, we obtain  $\hat{\xi} < 1$  for nearly all propagation directions. For B-models, the situation is the opposite. The SH waves have lower velocities than SV waves in a significant azimuth interval for small dips whereas they are higher for large dips, with a 45° dip resulting in negligible anisotropy.

Figure 12d shows the  $\xi$  parameter as a function of dip of the  $a$ -axis or  $b$ -axis for cases where the velocities are averaged over azimuth, as in the present study. In this case,  $\xi$  has its usual meaning and represents the ratio of the average of  $\hat{L}$  and  $\hat{N}$  over all azimuths. Positive RA of at least  $\xi = 1.05$ , as required in this study, is achieved for A-models with a dip smaller than about 25° and for B-models with a dip larger than 60°, assuming complete alignment and 59% olivine as in our petrological model.

### 5.3. Are Our Results Consistent With Other Anisotropy Studies in Fennoscandia?

The lithospheric anisotropy in Fennoscandia has been analyzed in several comprehensive studies. Analyzing Love and Rayleigh waves propagating between KEV and LVZ stations in an East-West backazimuth in the northern part of our study region, Lebedev et al. (2009) observed a velocity difference corresponding to a  $\xi$  value of 1.06.

Another study pertaining directly to RA is the body-wave tomography by Eken et al. (2008). They derived separate SH-wave and SV-wave models by analysis of SV and SH body-wave residuals at the stations of the Swedish Seismological National Network (SSNN), overlapping with a large section of our network. Observations of distinct SH and SV wave arrivals and not of fast and slow waves with more general polarizations suggest RA or anisotropy with symmetry along the NE-SW dominant backazimuth direction of their events. In our Central region, from 61 to 64°N, their velocity difference corresponds to a  $\xi$  value of up to 1.04 down to 200 km depth, in good correspondence with our results. North of this line, they observed a rather negative RA.

Eken et al. (2010) analyzed SKS splitting and P-wave residuals at the SSNN stations and inverted them jointly assuming A-models or B-models. They conclude that P-residuals alone cannot distinguish between A-models and B-models, but that the introduction of SKS-splitting information clearly favor B-models in four of the five geographical regions they have identified, with the dip of the  $b$ -axis mostly from 20° to 35°, with the exception of a smaller region with dip of 70°. Plomerová et al. (2011) also combine P-residuals and SKS-splitting in a region that corresponds to the northern part of our study region. They also favor B-models with small dips.

In the northern region, Vinnik et al. (2014) combined SKS-splitting with P-receiver functions to derive the depth of the anisotropy. They consider only A-models with horizontal  $a$ -axis in their modeling but examine the possibility of B-models in the discussion and note that horizontal  $b$ -axis is a tectonically plausible model for their observations. They find that the SKS-splitting signal has both an upper lithospheric component with 3% anisotropy in S-wave velocity down to 120 km depth and a separated weaker sub-lithospheric component at 200 km depth. This is consistent with the amplitude and more shallow RA in our model in the northern region.

Splitting of SKS and other core phases at the ScanArray stations has been analyzed by Grund and Ritter (2020). They observe a large number of stations with null splitting (due to the limited azimuthal range not necessarily implying the absence of anisotropy) in the central region and along the coast further north. B-models with very large dip would actually produce positive RA but no significant splitting (green case in Figure 12b). In the south, they observe rather simple splitting patterns at most stations, with delays around 1 s, but with different directions of the fast axis at the scale of our southern region. Lateral variation of the fast direction at such a scale would be seen as simple positive RA by long-period surface waves. Further east and north east, in the oldest domains, they observe a more complex pattern that is not well explained by two layers of anisotropy but fits well with dipping  $a$ -axes. The inferred dip is rather large, with values between 65° and 75° at 37 of the 45 stations involved, which would result in negative RA. The lateral variation in their results is in contrast with the rather homogeneous  $\xi$  values found in the present work, but the resolution and sensitivity of the two types of waves to elastic parameters are very different, and the two models are at least compatible in our central and south regions.

Neither in Paper I nor in the present study do we resolve any azimuthal variation of the surface wave phase velocities compatible with anisotropy. B-models with significant dip (red and green curves in the right plots of Figure 12b) are associated with much smaller azimuthal velocity variations than A-models with little dip. B-models are therefore more appropriate to reconcile positive RA with the absence of a large  $\pi$ -azimuthal

variation in the Rayleigh wave phase velocities, as would be expected from a-axis orientation in a single horizontal direction. This variation can however be masked by the other effects related to lateral variations which we have discussed in the previous section.

Summarizing these different studies, it is clear that anisotropy is prevalent in Fennoscandia, but is not uniform and simple. Dipping axes are suggested in several studies. B-models are favored for explaining P residuals, but their consistency with non-zero cases of SKS-splitting requires a small dip that would not produce the positive RA observed here, unless SKS waves are split by sub-lithospheric anisotropy, as partly observed in the North (Vinnik et al., 2014). As these different studies have very different resolutions, a joint analysis of all the available data would be beneficial to conduct.

## 6. Conclusion

Joint inversion of the phase velocity of Rayleigh and Love waves from teleseismic events reveals the presence of positive RA in Fennoscandia with  $\xi$  of about 1.05 from the Moho to at least 200 km depth, with no significant difference from North to South. This corresponds to SH wave velocities about 2.5% faster than SV waves velocities. We compare different approaches of determining azimuthally averaged phase velocities and evaluate confidence intervals to ensure the observed RA is well resolved. We also show that possible artifacts in measurements of the phase velocities related to lateral heterogeneities or interferences do not provide suitable alternative explanations to the observed Love-Rayleigh discrepancy.

Positive RA is commonly found in the continental lithosphere with  $\xi$  values similar to those observed in this study. Clustering of global RA in Lekic and Romanowicz (2011) shows, for example, an average values of  $\xi = 1.05$  from 50 to 200 km depth in their cluster corresponding to the continental lithosphere. Recent regional studies with very similar values and depth distributions include Calo et al. (2016) for North America and Ravenna et al. (2018) for southern Africa. Similar positive RA is also observed in Australia, although somewhat deeper (Khan et al., 2013).

The continental lithospheric anisotropy is more challenging to interpret than the oceanic one due to the complex tectonic history and the variety of deformation mechanisms this lithosphere has sustained. Although CPO, ubiquitous in natural samples of the continental lithosphere, is clearly the most plausible cause of the anisotropy, it is often difficult to reconcile different observations with a single model, as we also show for Fennoscandia. Horizontal orientation of the olivine *a*-axis in random azimuths can explain the global scale sub-Moho continental RA, as noted for example, by Becker et al. (2008). We show that AG-type CPO which orients the olivine *b*-axis perpendicularly to the compression direction is an interesting alternative to *a*-axis orientation models to explain continental RA. This kind of CPO is very common in continentally derived natural samples (Bernard et al., 2019). We show that the *b*-axis has to be oriented with a dip of at least 60° with respect to the horizontal plane to produce a positive RA of 1.05, as opposed to the *a*-axis models which require a dip of the *a*-axis not more than 25°. This alternative CPO model requires therefore a rather vertical direction of compression if the anisotropy is created by relatively recent compression, but a more horizontal direction of compression is also possible if frozen-in anisotropy is subsequently tilted during tectonic processes.

## Data Availability Statement

The values of the Rayleigh and Love wave phase velocities and the  $\xi$  and  $V_{SV}$  models presented in Figure 11 are provided in Supporting Information. The authors thank the GEOFON data center of the GFZ (German Research Centre for Geosciences) for archiving the ScanArrayCore data. Other data were downloaded from the European Integrated Data Archive (EIDA). Seismic data from the following networks were used: ScanArrayCore 1G-2012 (Thybo et al., 2012); NEONOR2 2D-2013 ([https://www.fdsn.org/networks/detail/2D\\_2013/](https://www.fdsn.org/networks/detail/2D_2013/)); SCANLIPS3D ZR-2013 (England et al., 2015); Swedish National Seismic Network UP (SNSN, 1904); Finnish National Seismic Network HE (Institute of Seismology University of Helsinki, 1980); Northern Finland Seismic Network FN (<https://geofon.gfz-potsdam.de/waveform/archive/network.php?ncode=FN>); Danish National Seismic Network (<https://geofon.gfz-potsdam.de/waveform/archive/network.php?ncode=DKDK>), NORSAR (NO (NORSAR, 1971), Norwegian National Seismic Network NS (University of Bergen, 1982)), and Global

Seismograph Network IU (Albuquerque Seismological Laboratory (ASL)/USGS, 1988). Figures were prepared with Matlab, except for Figure 1 which was created with GMT (Wessel et al., 2013).

### Acknowledgments

Insightful reviews by Vadim Levin, an anonymous reviewer and the associate editor are greatly appreciated. VM acknowledges support from the Research Council of Norway through its Centers of Excellence funding scheme, Project number 223272. The research has also been supported by grants TI-316/3-1 and -2) of the Deutsche Forschungsgemeinschaft.

### References

- Albuquerque Seismological Laboratory (ASL)/USGS. (1988). *Global Seismograph Network – IRIS/USGS International Federation of Digital Seismograph Networks*. Dataset/Seismic Network. <https://doi.org/10.7914/SN/IU>
- Alder, C., Bodin, T., Ricard, Y., Capdeville, Y., Debayle, E., & Montagner, J. P. (2017). Quantifying seismic anisotropy induced by small-scale chemical heterogeneities. *Geophysical Journal International*, 211(3), 1585–1600. <https://doi.org/10.1093/gji/ggx389>
- Artemieva, I. (2019). Lithosphere structure in Europe from thermal isostasy. *Earth-Science Reviews*, 188, 454–468. <https://doi.org/10.1016/j.earscirev.2018.11.004>
- Auer, L., Boschi, L., Becker, T. W., Nissen-Meyer, T., & Giardini, D. (2014). Savani: A variable resolution whole-mantle model of anisotropic shear velocity variations based on multiple data sets. *Journal of Geophysical Research: Solid Earth*, 119(4), 3006–3034. <https://doi.org/10.1002/2013JB010773>
- Ave Lallemand, H., & Carter, N. (1970). Syntectonic recrystallization of olivine and modes of flow in upper mantle. *The Geological Society of America Bulletin*, 81(8), 2203–2220. [https://doi.org/10.1130/0016-7606\(1970\)81\[2203:SROOAM\]2.0.CO;2](https://doi.org/10.1130/0016-7606(1970)81[2203:SROOAM]2.0.CO;2)
- Backus, G. (1962). Long-wave elastic anisotropy produced by horizontal layering. *Journal of Geophysical Research*, 67(11), 4427–4440. <https://doi.org/10.1029/JZ067i011p04427>
- Becker, T. W., Kustowski, B., & Ekström, G. (2008). Radial seismic anisotropy as a constraint for upper mantle rheology. *Earth and Planetary Science Letters*, 267(1–2), 213–227. <https://doi.org/10.1016/j.epsl.2007.11.038>
- Beghein, C., Trampert, J., & van Heijst, H. (2006). Radial anisotropy in seismic reference models of the mantle. *Journal of Geophysical Research: Solid Earth*, 111(B2), B02303. <https://doi.org/10.1029/2005JB003728>
- Ben Ismail, W., & Mainprice, D. (1998). An olivine fabric database: An overview of upper mantle fabrics and seismic anisotropy. *Tectonophysics*, 296(1–2), 145–157.
- Bernard, R., Behr, W., Becker, T., & Young, D. (2019). Relationships between olivine CPO and deformation parameters in naturally deformed rocks and implications for mantle seismic anisotropy. *Geochemistry, Geophysics, Geosystems*, 20(7), 3469–3494. <https://doi.org/10.1029/2019GC008289>
- Calo, M., Bodin, T., & Romanowicz, B. (2016). Layered structure in the upper mantle across North America from joint inversion of long and short period seismic data. *Earth and Planetary Science Letters*, 449, 164–175. <https://doi.org/10.1016/j.epsl.2016.05.054>
- Demouchy, S., Mussi, A., Barou, F., Tommasi, A., & Cordier, P. (2014). Viscoplasticity of polycrystalline olivine experimentally deformed at high pressure and 900 degrees C. *Tectonophysics*, 623, 123–135. <https://doi.org/10.1016/j.tecto.2014.03.022>
- Dziewonski, A., & Anderson, D. (1981). Preliminary reference Earth model. *Earth and Planetary Science Letters*, 25, 297–356. [https://doi.org/10.1016/0031-9201\(81\)90046-7](https://doi.org/10.1016/0031-9201(81)90046-7)
- Eken, T., Plomerova, J., Roberts, R., Vecsey, L., Babuska, V., Shomali, H., & Bodvarsson, R. (2010). Seismic anisotropy of the mantle lithosphere beneath the Swedish National Seismological Network (SNSN). *Tectonophysics*, 480(1–4), 241–258. <https://doi.org/10.1016/j.tecto.2009.10.012>
- Eken, T., Plomerova, J., Vecsey, L., Babuska, V., Roberts, R., Shomali, H., & Bodvarsson, R. (2012). Effects of seismic anisotropy on P-velocity tomography of the Baltic Shield. *Geophysical Journal International*, 188(2), 600–612. <https://doi.org/10.1111/j.1365-246X.2011.05280.x>
- Eken, T., Shomali, Z. H., Roberts, R., Hieronymus, C. F., & Bodvarsson, R. (2008). S and P velocity heterogeneities within the upper mantle below the Baltic Shield. *Tectonophysics*, 462(1–4), 109–124. <https://doi.org/10.1016/j.tecto.2008.02.015>
- England, R. W., & Ebbing, J. (2012). Crustal structure of central Norway and Sweden from integrated modelling of teleseismic receiver functions and the gravity anomaly. *Geophysical Journal International*, 191(1), 1–11. <https://doi.org/10.1111/j.1365-246X.2012.05607.x>
- England, R. W., Ebbing, J., & Mansour, W. B. (2015). SCANLIPS3D – SCANDinavian Lithosphere P and S wave experiment 3 D.
- Estey, L., & Douglas, B. (1986). Upper mantle anisotropy – A preliminary model. *Journal of Geophysical Research-Solid Earth and Planets*, 91(B11), 1393–1406. <https://doi.org/10.1029/JB091iB11p11393>
- Foster, A., Nettles, M., & Ekström, G. (2014). Overtone interference in array-based love-wave phase measurements. *Bulletin of the Seismological Society of America*, 104(5), 2266–2277. <https://doi.org/10.1785/0120140100>
- French, S. W., & Romanowicz, B. A. (2014). Whole-mantle radially anisotropic shear velocity structure from spectral-element waveform tomography. *Geophysical Journal International*, 199(3), 1303–1327. <https://doi.org/10.1093/gji/ggu334>
- Freybourger, M., Gaherty, J. B., & Jordan, T. H. (2001). Structure of the Kaapvaal craton from surface waves. *Geophysical Research Letters*, 28(13), 2489–2492. <https://doi.org/10.1029/2000GL012436>
- Gaherty, J. B. (2004). A surface wave analysis of seismic anisotropy beneath eastern North America. *Geophysical Journal International*, 158(3), 1053–1066. <https://doi.org/10.1111/j.1365-246X.2004.02371.x>
- Grund, M., & Ritter, J. R. R. (2020). Shear-wave splitting beneath Fennoscandia – Evidence for dipping structures and laterally varying multilayer anisotropy. *Geophysical Journal International*, 223(3), 1525–1547. <https://doi.org/10.1093/gji/ggaa388>
- Hansen, L., Faccenda, M., & Warren, J. (2021). A review of mechanisms generating seismic anisotropy in the upper mantle. *Physics of the Earth and Planetary Interiors*, 313, 106662. <https://doi.org/10.1016/j.pepi.2021.106662>
- Hansen, L., Qi, C., & Warren, J. (2016). Olivine anisotropy suggests Gutenberg discontinuity is not the base of the lithosphere. *Proceedings of the National Academy of Sciences of the United States of America*, 113(38), 10503–10506. <https://doi.org/10.1073/pnas.1608269113>
- Hariharan, A., Dalton, C., Babikoff, J., & Ekström, G. (2022). Controls on surface wave overtone interference. *Geophysical Journal International*, 228(3), 1665–1683. <https://doi.org/10.1093/gji/ggab424>
- Institute of Seismology University of Helsinki. (1980). The Finnish National Seismic Network. Deutsches GeoForschungsZentrum GFZ. Other/ Seismic Network. <https://doi.org/10.14470/UR044600>
- Karato, S., Jung, H., Katayama, I., & Skemer, P. (2008). Geodynamic significance of seismic anisotropy of the upper mantle: New insights from laboratory studies. *Annual Review of Earth and Planetary Sciences*, 36, 59–95. <https://doi.org/10.1146/annurev.earth.36.031207.124120>
- Kennett, B. L. N., Engdahl, E. R., & Buland, R. (1995). Constraints on seismic velocities in the Earth from traveltimes. *Geophysical Journal International*, 122(1), 108–124. <https://doi.org/10.1111/j.1365-246X.1995.tb03540.x>
- Khan, A., Zunino, A., & Deschamps, F. (2013). Upper mantle compositional variations and discontinuity topography imaged beneath Australia from Bayesian inversion of surface-wave phase velocities and thermochemical modeling. *Journal of Geophysical Research: Solid Earth*, 118(10), 5285–5306. <https://doi.org/10.1002/jgrb.50304>

- Köhler, A., Maupin, V., & Balling, N. (2015). Surface wave tomography across the Sorgenfrei-Tornquist Zone, SW Scandinavia, using ambient noise and earthquake data. *Geophysical Journal International*, 203(1), 284–311. <https://doi.org/10.1093/gji/ggv297>
- Kolínský, P., & Bokelmann, G., & the AlpArray Working Group. (2021). On the wobbles of phase-velocity dispersion curves. *Geophysical Journal International*, 224(3), 1477–1504. <https://doi.org/10.1093/gji/ggaa487>
- Laske, G., & Widmer-Schmidrig, R. (2015). Theory and observations – Normal modes and surface waves measurements. In *Treatise on geophysics* (pp. 67–125). Elsevier.
- Lavoué, F., Lebedev, S., Celli, N., & Schaeffer, A. (2021). Radially and azimuthally anisotropic shear-wave velocity model of the Earth's upper mantle. In *EGU General Assembly 2021* (p. EGU21-14987). <https://doi.org/10.5194/egusphere-egu21-14987>
- Lebedev, S., Boonen, J., & Trampert, J. (2009). Seismic structure of Precambrian lithosphere: New constraints from broad-band surface-wave dispersion. *Lithos*, 109(1–2), 96–111. <https://doi.org/10.1016/j.lithos.2008.06.010>
- Lekic, V., & Romanowicz, B. (2011). Tectonic regionalization without a priori information: A cluster analysis of upper mantle tomography. *Earth and Planetary Science Letters*, 308(1–2), 151–160. <https://doi.org/10.1016/j.epsl.2011.05.050>
- Lévêque, J., Cara, M., & Rouland, D. (1991). Waveform inversion of surface wave data: Test of a new tool for systematic investigation of upper mantle structures. *Geophysical Journal International*, 104(3), 565–581.
- Lévêque, J., Debayle, E., & Maupin, V. (1998). Anisotropy in the Indian Ocean upper mantle from Rayleigh and Love waveform inversion. *Geophysical Journal International*, 133(3), 529–540. <https://doi.org/10.1046/j.1365-246X.1998.00504.x>
- Levshin, A., Pisarenko, V., & Pogrebinsky, G. (1972). On a frequency-time analysis of oscillations. *Annals of Geophysics*, 28, 211–218.
- Magali, J., Bodin, T., Hedjazian, N., Ricard, Y., Capdeville, Y., & Debayle, E. (2021). Quantifying intrinsic and extrinsic contributions to radial anisotropy in tomographic models. *Journal of Geophysical Research: Solid Earth*, 126(10), e2021JB022322. <https://doi.org/10.1029/2021JB022322>
- Mauerberger, A., Maupin, V., Gudmundsson, O., & Tilmann, F. (2021). Anomalous azimuthal variations with 360 degrees periodicity of Rayleigh phase velocities observed in Scandinavia. *Geophysical Journal International*, 224(3), 1684–1704. <https://doi.org/10.1093/gji/ggaa553>
- Mauerberger, A., Maupin, V., Sadeghisorkhani, H., Gudmundsson, O., & Tilmann, F. (2022). A shear-wave velocity model for the Scandinavian lithosphere from Rayleigh waves and ambient noise – Implications for the origin of the topography of the Scandes mountain range. *Tectonophysics*, 838, 229507. <https://doi.org/10.1016/j.tecto.2022.229507>
- Maupin, V. (2002). The amplitude of the Love-Rayleigh discrepancy created by small-scale heterogeneities. *Geophysical Journal International*, 150(1), 58–64. <https://doi.org/10.1046/j.1365-246X.2002.01676.x>
- Maupin, V. (2011). Upper-mantle structure in southern Norway from beamforming of Rayleigh wave data presenting multipathing. *Geophysical Journal International*, 185(2), 985–1002. <https://doi.org/10.1111/j.1365-246X.2011.04989.x>
- Maupin, V., & Cara, M. (1992). Love-Rayleigh wave incompatibility and possible deep upper mantle anisotropy in the Iberian Peninsula. *Pure and Applied Geophysics*, 138(3), 429–444. <https://doi.org/10.1007/bf00876881>
- Maupin, V., & Park, J. (2015). Theory and observations – Seismic anisotropy. In *Treatise on geophysics* (pp. 277–305). Elsevier. <https://doi.org/10.1016/B978-0-444-53802-4.00007-5>
- Menzel, D. (1961). *Mathematical physics*. Dover Publications.
- Montagner, J. P., & Nataf, H. (1986). A simple method for inverting the azimuthal anisotropy of surface-waves. *Journal of Geophysical Research-Solid Earth and Planets*, 91(B1), 511–520. <https://doi.org/10.1029/JB091iB01p00511>
- Moulik, P., & Ekström, G. (2014). An anisotropic shear velocity model of the Earth's mantle using normal modes, body waves, surface waves and long-period waveforms. *Geophysical Journal International*, 199(3), 1713–1738. <https://doi.org/10.1093/gji/ggu356>
- Nataf, H., Nakanishi, I., & Anderson, D. (1984). Anisotropy and shear-wave velocity heterogeneities in the upper mantle. *Geophysical Research Letters*, 11(2), 109–112. <https://doi.org/10.1029/GL011i002p00109>
- Nettles, M., & Dziewonski, A. (2011). Effect of higher-mode interference on measurements and models of fundamental-mode surface-wave dispersion. *Bulletin of the Seismological Society of America*, 101(5), 2270–2280. <https://doi.org/10.1785/0120110019>
- Nettles, M., & Dziewonski, A. M. (2008). Radially anisotropic shear velocity structure of the upper mantle globally and beneath North America. *Journal of Geophysical Research: Solid Earth*, 113(B2), B02303. <https://doi.org/10.1029/2006JB004819>
- Nicolas, A., Boudier, F., & Boullier, A. (1973). Mechanisms of flow in naturally and experimentally deformed peridotites. *American Journal of Science*, 273(10), 853–876. <https://doi.org/10.2475/ajs.273.10.853>
- NORSAR. (1971). NORSAR Station Network. [Dataset]. NORSAR. <https://doi.org/10.21348/d.no.0001>
- Olsson, S., Roberts, R. G., & Bödvarsson, R. (2008). Moho depth variation in the Baltic Shield from analysis of converted waves. *GFF*, 130(3), 113–122. <https://doi.org/10.1080/11035890809453227>
- Pedersen, H. A., Bruneton, M., & Maupin, V. (2006). Lithospheric and sublithospheric anisotropy beneath the Baltic shield from surface-wave array analysis. *Earth and Planetary Science Letters*, 244(3), 590–605. <https://doi.org/10.1016/j.epsl.2006.02.009>
- Plomerová, J., Vecsey, L., Babuška, V., & Group, L. W. (2011). Domains of Archean mantle lithosphere deciphered by seismic anisotropy – Inferences from the LAPNET array in northern Fennoscandia. *Solid Earth*, 2(2), 303–313. <https://doi.org/10.5194/se-2-303-2011>
- Ravenna, M., Lebedev, S., Fulla, J., & Adam, J. M.-C. (2018). Shear-wave velocity structure of southern Africa's lithosphere: Variations in the thickness and composition of cratons and their effect on topography. *Geochemistry, Geophysics, Geosystems*, 19(5), 1499–1518. <https://doi.org/10.1029/2017GC007399>
- Saito, M. (1988). Disper80: A subroutine package for the calculation of seismic normal mode solutions. In D. Doornbos (Ed.), *Seismological algorithms: Computational methods and computer programs* (pp. 293–319). Academic Press.
- Schaeffer, A. J., Lebedev, S., & Becker, T. W. (2016). Azimuthal seismic anisotropy in the Earth's upper mantle and the thickness of tectonic plates. *Geophysical Journal International*, 207(2), 901–933. <https://doi.org/10.1093/gji/ggw309>
- Smith, M., & Dahlen, F. (1973). Azimuthal dependence of love and Rayleigh-wave propagation in a slightly anisotropic medium. *Journal of Geophysical Research*, 78(17), 3321–3333. <https://doi.org/10.1029/JB078i017p03321>
- SNSN. (1904). *Swedish National Seismic Network*. Uppsala University. <https://doi.org/10.18159/SNSN>
- Tanimoto, T., & Anderson, D. (1985). Lateral heterogeneity and azimuthal anisotropy of the upper mantle – Love and Rayleigh-waves 100–250 S. *Journal of Geophysical Research-Solid Earth and Planets*, 90(NB2), 1842–1858. <https://doi.org/10.1029/JB090iB02p01842>
- Tarantola, A., & Valette, B. (1982). Generalized nonlinear inverse problems solved using the least squares criterion. *Reviews of Geophysics*, 20(2), 219–232. <https://doi.org/10.1029/RG020i002p00219>
- Thybo, H., Balling, N., Maupin, V., Ritter, J. R. R., & Tilmann, F. (2012). ScanArray core (1G 2012–2017). The ScanArray consortium. <https://doi.org/10.14470/6T569239>
- Thybo, H., Bulut, N., Grund, M., Mauerberger, A., Makushkina, A., Artemieva, I. M., et al. (2021). ScanArray—A broadband seismological experiment in the Baltic shield. *Seismological Research Letters*, 92(5), 2811–2823. <https://doi.org/10.1785/0220210015>

- Tommasi, A., & Vauchez, A. (2015). Heterogeneity and anisotropy in the lithospheric mantle. *Tectonophysics*, *661*, 11–37. <https://doi.org/10.1016/j.tecto.2015.07.026>
- University of Bergen. (1982). University of Bergen Seismic Network (Data set). <https://doi.org/10.7914/SN/NS>
- Vinnik, L., Oreshin, S., Makeyeva, L., Peregoudov, D., Kozlovskaya, E., & The POLENET/LAPNET WG. (2014). Anisotropic lithosphere under the Fennoscandian shield from P receiver functions and SKS waveforms of the POLENET/LAPNET array. *Tectonophysics*, *628*, 45–54. <https://doi.org/10.1016/j.tecto.2014.04.024>
- Wang, N., Montagner, J.-P., Fichtner, A., & Capdeville, Y. (2013). Intrinsic versus extrinsic seismic anisotropy: The radial anisotropy in reference Earth models. *Geophysical Research Letters*, *40*(16), 4284–4288. <https://doi.org/10.1002/grl.50873>
- Wessel, P., Smith, W., Scharroo, R., Luis, J., & Wobbe, F. (2013). Generic mapping tools: Improved version released. *Eos Transactions American Geophysical Union*, *94*, 409–410. <https://doi.org/10.1002/2013eo450001>
- Wielandt, E. (1993). Propagation and structural interpretation of non-plane waves. *Geophysical Journal International*, *113*(1), 45–53. <https://doi.org/10.1111/j.1365-246X.1993.tb02527.x>
- Wielandt, E., & Schenk, H. (1983). On systematic errors in phase velocity analysis. *Journal of Geophysics-Zeitschrift für Geophysik*, *52*(1), 1–6.
- Wielandt, E., Sigg, A., Plesinger, A., & Horalek, J. (1987). Deep-structure of the Bohemian Massif from phase velocities of Rayleigh and love waves. *Studia Geophysica et Geodaetica*, *31*(1), 1–7. <https://doi.org/10.1007/BF01631100>
- Zhang, J., Bass, J., & Schmandt, B. (2018). The elastic anisotropy change near the 410-km discontinuity: Predictions from single-crystal elasticity measurements of olivine and wadsleyite. *Journal of Geophysical Research: Solid Earth*, *123*(4), 2674–2684. <https://doi.org/10.1002/2017JB015339>